Supporting Information

Stepwise assembly of thiacalix[4]arene-protected Ag/Ti bimetallic nanoclusters: Accurate identification of catalytic Ag sites in CO$_2$ electroreduction

Yi-Qi Tian,[a] Wen-Lei Mu,[a] Lin-Lin Wu,*[a] Xiao-Yi Yi,[a] Jun Yan,*[a] Chao Liu*[a]

a Hunan Provincial Key Laboratory of Chemical Power Sources, College of Chemistry and Chemical Engineering, Central South University, Changsha 410083, Hunan, P. R. China

Abstract: Accurate identification of catalytic sites of heterogeneous catalysts is difficult because of the difficulty in controlling interfacial chemistry at the molecular level. Here, the thiacalix[4]arene (TC4A)-protected Ti–oxo core has for the first time been used as a template for loading Ag^{1+} ions, and a novel Ag/Ti bimetallic nanocluster of **Ti$_8$Ag$_8$**, with multiple surface-exposed Ag sites, has thereby been synthesized. The **Ti$_8$Ag$_8$** contained a "core–shell" {Ti$_4$@Ag$_8$(TC4A)$_4$} cluster that consisted of a {Ti$_2$O$_2$@Ag$_4$(TC4A)$_2$} and two {Ti@Ag$_2$(TC4A)} motifs. For comparison, a **Ti$_2$Ag$_4$** cluster with the same structure as {Ti$_2$O$_2$@Ag$_4$(TC4A)$_2$} within **Ti$_8$Ag$_8$**, was also prepared. The structural differences between **Ti$_8$Ag$_8$** and **Ti$_2$Ag$_4$** provided a perfect platform for an accurate comparison of catalytic activity at different Ag sites. The **Ti$_8$Ag$_8$** showed an excellent activity for the electroreduction CO$_2$ reduction reaction (eCO$_2$RR) with a CO faradaic efficiency (FE$_{CO}$) of 92.33% at −0.9 V vs RHE, which was much higher than that of **Ti$_2$Ag$_4$** (FE$_{CO}$ = 69.87% at −0.8 V vs RHE). Density functional theory (DFT) calculations revealed the catalytic mechanism, and also disclosed that Ag active sites located at {Ti@Ag$_2$(TC4A)} present a higher ε$_d$ value than those at {Ti$_2$O$_2$@Ag$_4$(TC4A)$_2$}, which could better stabilize the *COOH intermediate in eCO$_2$RR.

Contents

1. Experimental section

Materials and Characterization. All reagents were purchased commercially and were not further purified when used. Powder X-ray diffraction (PXRD) analysis were performed on a Rigaku Mini Flex II diffractometer at a 2θ range of 3–50° (5° min^{-1}) with CuK$_\alpha$ radiation (λ =1.54056 Å). The solid-state UV/Vis spectra data of the cluster samples were obtained on UV-4000 spectrophotometer. Electrospray ionization mass spectrometry (ESI-MS) were performed on a Bruker Daltonik GmbH (Bruker, Germany). Thermogravimetric (TGA) patterns were recorded on a Mettler Toledo TGA/SDTA 851e analyzer in a N$_2$ atmosphere. FT-IR spectra using KBr pellets were taken on a Bruker Vertex 70 Spectrometer. Transmission electron microscope (TEM) images and EDX were measured using FEI Tecnai F20. XPS analysis was performed on a Physical Electronics Quantum 2000 instrument equipped with a monochromatic Al Kα source (Kα = 1486.6 eV) at 300 W under ultrahigh vacuum. The binding energy (BE) values were referenced to the C1s peak of adventitious carbon, which is conventionally set at 284.6 eV.

X-ray Crystal Structure Determination. Single crystal diffraction data for the **Ti$_8$Ag$_8$** was collected on Bruker D8 Venture diffractometer with liquid metal Ga K$_\alpha$ radiation. Single crystal diffraction data for the **Ti$_1$Ag$_1$**, **Ti$_2$Ag$_2$**, **Ti$_2$Ag$_{2.6}$** and **Ti$_2$Ag$_4$** were conducted on Rigaku XtalAB Synergy DS diffractometer with Cu K$_\alpha$ radiation. The date was solved using intrinsic phasing methods in ShelXT program and then refined by full-matrix least-squares on F2 using ShelXL-2014 in Olex^2 program. The hydrogen atoms were introduced at their geometric positions and refined as riding atom, and the positions of non-hydrogen atoms were refined with anisotropic displacement parameters during the final cycles. Due to the rotation disorder of tert-butyl groups, in all cases the ISOR, DELU and SIMU constraints were necessary to achieve convergence. The SQUEEZE operation was used to eliminate the contribution of disordered solvent molecule to the reflection intensity. A summary of the crystallographic data for the reported clusters is listed in Table S1. CCDC **2262773-2262777** contain the crystallographic data herein.

Synthesis for compound {TiAg(TC4A)[P(Ph)$_3$]$_2$(O^{i}Pr)DMF} Ti$_1$Ag$_1$

TC4A (23 mg, 0.032 mmol), triphenylphosphine (26.2 mg, 0.1 mmol) and silver acetate (16.7 mg, 0.1 mmol) were added in a 15mL glass bottles with mixed solvent of HO^{i}Pr and DMF (6mL, v:v=1:1). Ti(O^{i}Pr)$_4$ (200 μL, 0.33 mmol) and three drop triethylamine were added dropwise. The resulting mixtures were sonicated for 5 min, then were transferred to a preheated oven at 80 °C for 2 days. Yellow colored crystals were obtained after cooling to 25 °C in a yield of ~80% (based on TC4A).

Synthesis for compound {Ti$_2$Ag$_2$(TC4A)$_2$(μ$_2$-O)(DMF)$_2$} Ti$_2$Ag$_2$

TC4A (23 mg, 0.032 mmol), phosphorous acid (41 mg, 0.5 mmol) and silver acetate (16.7 mg, 0.1 mmol) were added in a 15mL glass bottles with CH$_3$CN and DMF (3mL, v:v=2:1). Ti(O^{i}Pr)$_4$ (100 μL, 0.33 mmol) was added dropwise. The resulting mixtures were then transferred to a preheated oven at 80 °C for 2 days. Yellow colored crystals were obtained after cooling to 25 °C in a yield of ~35% (based on TC[4]A).

Synthesis for compound {Ti$_2$Ag$_{2.6}$(TC4A)$_2$(μ$_2$-O)(O^{i}Pr)$_2$} Ti$_2$Ag$_{2.6}$

TC4A (23 mg, 0.032 mmol), phosphorous acid (41 mg, 0.5 mmol) and silver acetate (16.7 mg, 0.1 mmol) were added in a 15mL glass tube with HO^{i}Pr (3mL). Ti(O^{i}Pr)$_4$ (100 μL, 0.33 mmol) was added dropwise. The resulting mixtures were then transferred to a preheated oven at 130 °C for 3 days. Yellow colored crystals were obtained after cooling to 25 °C in a yield of ~15% (based on TC4A).

Synthesis for compound {Ti$_2$Ag$_4$(TC4A)$_2$(μ$_2$-O)$_2$} Ti$_2$Ag$_4$

TC4A (23 mg, 0.032 mmol) and Silver trifluoroacetate (44 mg, 0.2 mmol) were added in a 15mL glass bottles with CH$_3$CN and DMF (3mL, v:v=2:1). Ti(O^{i}Pr)$_4$ (100 μL, 0.33 mmol) was added dropwise. The resulting mixtures were sonicated for 5 min, then were transferred to a preheated oven at 80 °C for 3 days. Yellow colored crystals were obtained after cooling to 25 °C in a yield of ~70% (based on TC4A).

Synthesis for compound {H$_7$Ti$_8$Ag$_8$NaO$_2$(TC4A)$_4$(Idc)$_6$(O^{i}Pr)$_{10}$(DMF)$_2$(H$_2$O)} Ti$_8$Ag$_8$

Method 1: TC4A (23 mg, 0.032 mmol), 4,5-Imidazoledicarboxylic acid (15.6 mg, 0.1mmol) and Silver trifluoroacetate (44 mg, 0.2 mmol) were added in a 15mL glass bottles with mixed solvent of ^{i}PrOH and DMF (2mL, v:v=1:2). Ti(O^{i}Pr)$_4$ (200 μL, 0.33 mmol) and three drop triethylamine were added dropwise. The resulting mixtures were sonicated for 5 min, then were transferred to a preheated oven at 80 °C for 2 days. Yellow colored crystals were obtained after cooling to 25 °C in a yield of ~45% (based on TC4A).

Method 2: TC4A (23 mg, 0.032 mmol), 4,5-Imidazoledicarboxylic acid (15.6 mg, 0.1mmol), Silver trifluoroacetate (44 mg, 0.2 mmol) and Sodium sulfate (1.42 mg 0.01 mmol) were added into a 25 mL Teflon lined stainless steel autoclave with mixed solvent of ^{i}PrOH and DMF (2mL, v:v=1:2). Ti(O^{i}Pr)$_4$ (200 μL, 0.33 mmol) and three drop triethylamine were added dropwise. The resulting mixtures were sonicated for 5 min, then were transferred to a preheated oven at 80 °C for 2 days. Yellow colored crystals were obtained after cooling to 25 °C in a yield of ~70% (based on TC[4]A).

Method 3: **Ti$_2$Ag$_4$** (10 mg, 0.032 mmol) and 4,5-Imidazoledicarboxylic acid (15.6 mg, 0.1mmol) were added in a 15mL glass bottles with mixed solvent of ^{i}PrOH and DMF (4mL, v:v=2:2). Ti(O^{i}Pr)$_4$ (200 μL, 0.33 mmol) and three drop triethylamine were added dropwise. The resulting mixtures were sonicated for 5 min, then were transferred to a preheated

oven at 80 °C for 2 days. Yellow colored crystals were obtained after cooling to 25 °C in a yield of ~10% (based on TC4A).
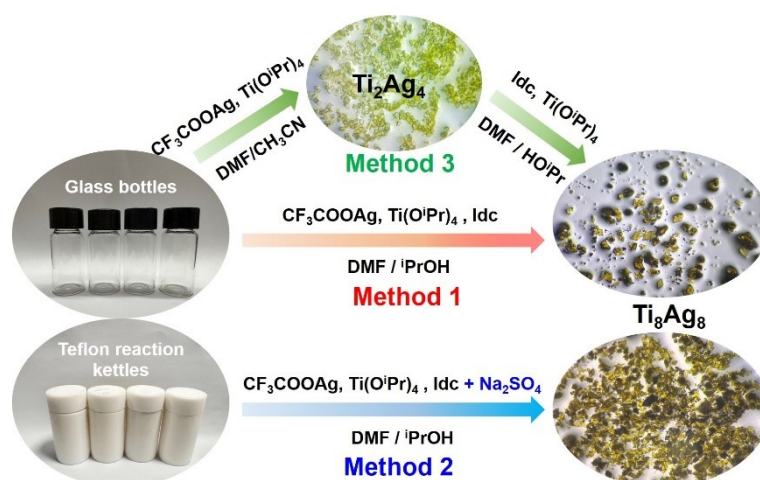
Scheme S1: Synthesis scheme of **Ti$_8$Ag$_8$**.

Electrochemical Measurements. The electrochemical performance was tested on CHI 660E (Shanghai) electrochemical workstation. All electrochemical measurements were carried out in a gas-tight H-cell separated by Nafion 117 membrane between the two compartments. Each part has 60 ml 0.5 M KHCO$_3$ electrolyte and 40 mL headspace. The test system uses a standard three-electrode system, an Ag/AgCl electrode is used as the reference electrode, carbon rod is the counter electrode, and catalysts modified carbon cloth electrodes were used as the working electrode. 100 μL catalysts suspension (20 wt% loading on acetylene black) and 0.5wt% Nafion solution were dropped on carbon cloth (1×1 cm^2). Before electrolysis measurement of CO$_2$ reduction, carbon dioxide was purged into the reaction system. Linear sweep voltammetry (LSV) was performed with a scan rate of 5 mV s^{-1} from 0 V to -1.2 V vs. Ag/AgCl in Ar-saturated and CO$_2$-saturated conditions. CO$_2$ atmosphere has been maintained during the testing process at rate of 20 mL/min. Gas phase products was analysis quantitatively using an Shimadzu GC-2014C Gas Chromatograph (Ar as gas carrier).ECSA measurement was estimated by performing cyclic voltammograms (CV) at different scan rates from 10 to 100 mV s^{-1} underthe potential window of −0.18 V to −0.06 V (vs. RHE) to measure the double-layer capacitance (C$_{dl}$). EIS measurement was carried out on the electrochemical analyzer in a frequency range from 100 kHz to 10 mHz at an overpotential of−0.90 V vs. RHE.

Computational details. Density functional theory (DFT) calculations are performed with Vienna *ab initio* simulation package (VASP 6.2.1).[1-4] The Perdew-Burke-Ernzerhof (PBE) functional is applied to describe the electronic exchange-correlation interaction.[5] The projector augmented-wave (PAW) method is employed to treat core-valence electron interaction.[6] The convergence criteria are set at 0.05 eV/Å for maximum forces as well as 1×10^{-5} eV for the relative energies. A cutoff energy of 460 eV is adopted for plane-wave basis sets. The lattice parameters of a= 38.3 Å, b= 38.4 Å and c= 38.0 Å are set to avoid the interaction among mirror images. Integration over the Brillouin zone was performed with a reciprocal space mesh consisting of only the Gamma point.[7] All atoms are allowed to relax during the structural optimization. The d-band center (ε$_d$) was calculated using Eq (1)

$$\varepsilon_d = \frac{\int_{-\infty}^{E_f} E\rho_d(E)dE}{\int_{-\infty}^{E_f} \rho_d(E)dE} \qquad (1)$$

Where ρ$_d$ represents the density of states projected onto the target metal's d band and E$_f$ is the Fermi energy.[8]

Reference

1. Kresse, G.; Joubert, D. From ultrasoft pseudopotentials to the projector augmented-wave method. *Physical Review B* 1999, **59**, 1758-1775.
2. Kresse, G.; Hafner, J. Ab initio molecular dynamics for liquid metals. *Physical Review B* 1993, **47**, 558-561.
3. Kresse, G.; Furthmüller, J. Efficient iterative schemes for ab initio total-energy calculations using a plane-wave basis set. *Physical Review B* 1996, **54**, 11169-11186.
4. Kresse, G.; Furthmüller, J. Efficiency of ab-initio total energy calculations for metals and semiconductors using a plane-wave basis set. Computational *Materials Science* 1996, **6**, 15-50.
5. Perdew, J. P.; Burke, K.; Ernzerhof, M. Generalized Gradient Approximation Made Simple. *Phys. Rev. Lett.* 1996, **77**, 3865-3868.
6. Blöchl, P. E. Projector augmented-wave method. *Physical Review B* 1994, **50**, 17953-17979.
7. Monkhorst, H. J.; Pack, J. D. Special points for Brillouin-zone integrations. *Physical Review B* 1976, **13**, 5188-5192.

8. Hammer, B.; Norskov, J. K. Theoretical surface science and catalysis-calculations and concepts. *Advances in Catalysis* 2000, **45**, 71–129.

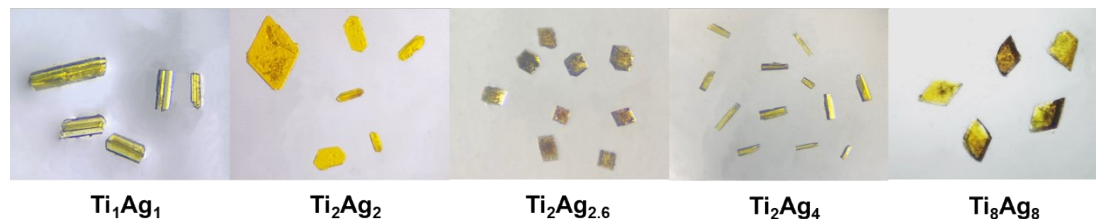## 2. Pictures of fresh crystals separated from the solution

| Ti_1Ag_1 | Ti_2Ag_2 | $Ti_2Ag_{2.6}$ | Ti_2Ag_4 | Ti_8Ag_8 |

Figure S1. Pictures of fresh crystals separated from the solution.

3. Structure of Compounds

Table S1. Crystallography Table of Compounds

Compounds	Ti_1Ag_1	Ti_2Ag_2	$Ti_2Ag_{2.6}$	Ti_2Ag_4	Ti_8Ag_8
CCDC	2262773	2262774	2262775	2262776	2262777
Formula	$C_{82}H_{88}NO_6S_4P_2$ $TiAg$	$C_{89}H_{109}N_3O_{12}S_8Ti_2Ag_2$	$C_{86}H_{100}O_{11}$ $S_8Ti_2Ag_{2.6}$	$C_{84}H_{94}N_2O_{10}S_8$ Ti_2Ag_4	$C_{220}H_{254}N_{13}O_{55}$ $S_{16}Ti_8Ag_8Na$
T(K)	150	150	150	150	150
F_w	1529.48	1906	1942.40	2075.37	5852
Crystal system	monoclinic	monoclinic	monoclinic	tetragonal	orthorhombic
Space group	$P2_1/c$	$P2_1/n$	$P2_1/c$	$P4_2/mcm$	$Pmn2_1$
a, Å	28.8480(12)	22.9703(13)	13.4327(4)	15.9991(4)	22.2730(15)
b, Å	11.2724(3)	15.9803(10)	19.1408(5)	15.9991(4)	44.470(3)
c, Å	25.8452(10)	36.153(3)	19.9855(6)	18.5546(12)	38.489(3)
$\alpha/°$	90	90	90	90	90
$\beta/°$	110.243(4)	95.010(7)	100.461(3)	90	90
$\gamma/°$	90	90	90	90	90
$V/Å^3$	7885.4(6)	13220.1(16)	5053.1(3)	4749.4(4)	38123(5)
Z	4	4	2	2	2
$\rho_{calcd}/gcm^{-3})$	1.288	0.995	1.277	1.451	1.000
μ/mm^{-1})	0.547	0.576	0.861	1.196	3.872
$F(000)$	3192.0	4104.0	1996.0	2104.0	11684.0
Reflections collected	27255	40452	44577	29248	392236
Data/restraints/parameters	27255/145/964	20834/1020/1194	9875/224/631	4597/56/154	55921/11107/4126
Goof	1.040	0.860	1.064	1.065	1.088
$R_1/wR_2(I> 2\sigma(I))$	0.0465/0.1125	0.0804/0.1950	0.0553/0.1332	0.0459/0.1176	0.0891/0.2203
R_1/wR_2(all data)	0.0969/0.1336	0.1518/0.2211	0.0753/0.1397	0.0969/0.1949	0.0969/0.2265
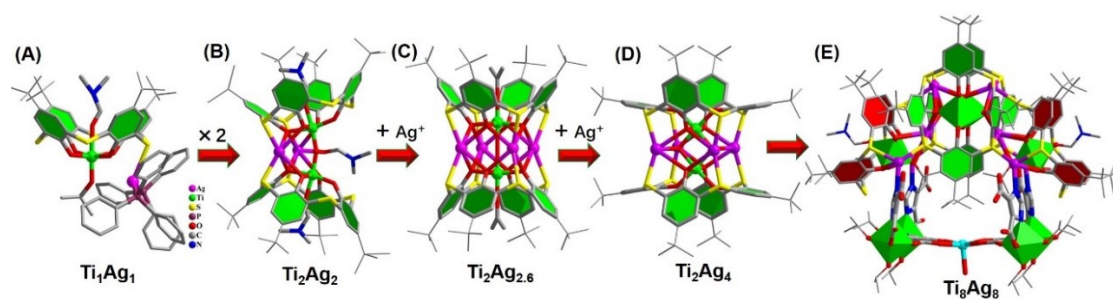
Figure S2. Stepwise assembly of thiacalix[4]arene-protected Ag/Ti bimetallic nanoclusters.
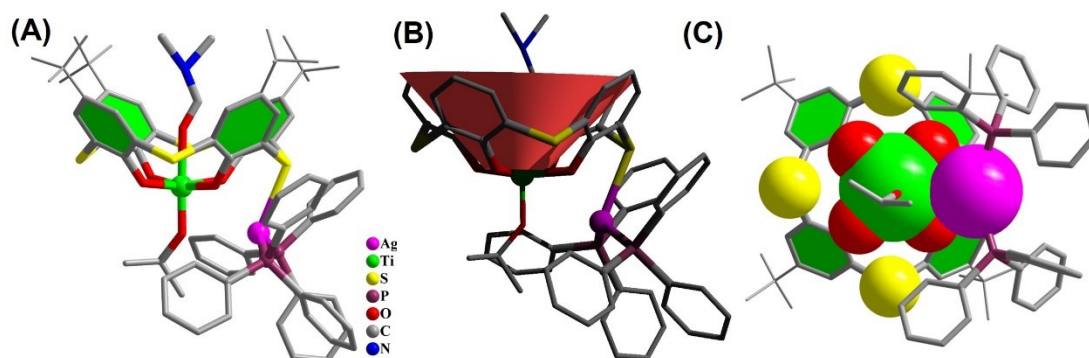
Figure S3. Molecular structures of the **Ti$_1$Ag$_1$**.
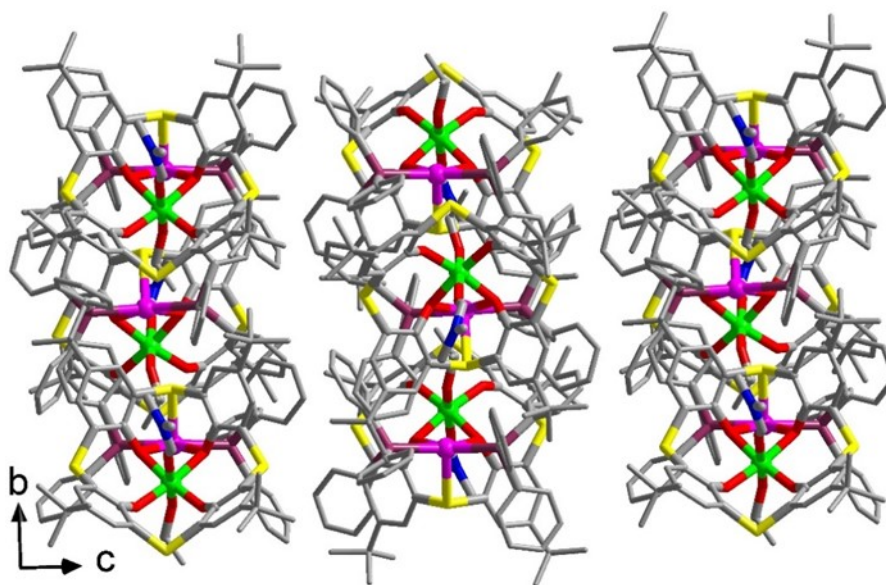
Figure S4. Three-dimensional packing structure of **Ti$_1$Ag$_1$** along the a axis.
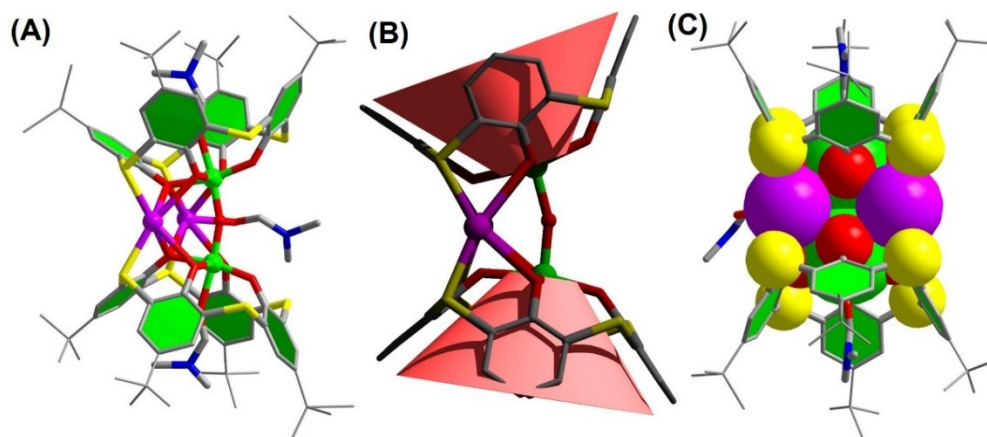
Figure S5. Molecular structures of **Ti$_2$Ag$_2$**.
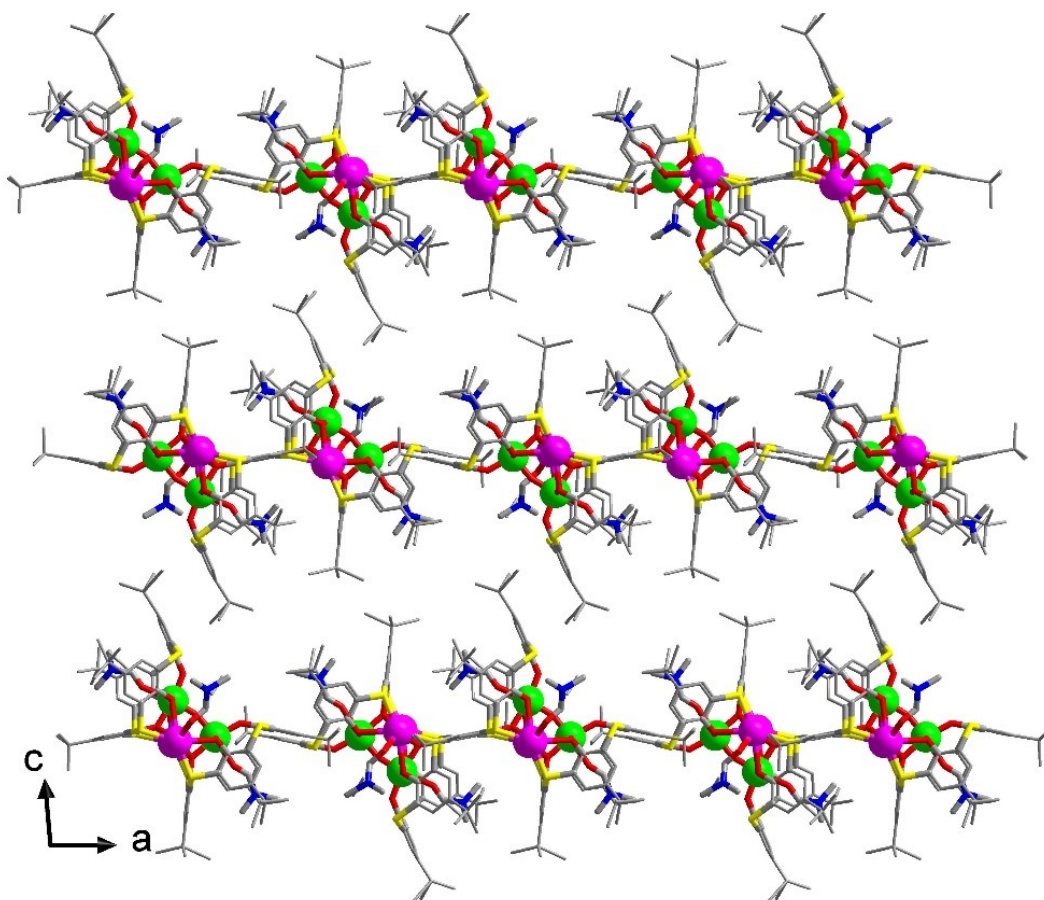
Figure S6. Three-dimensional packing structure of **Ti$_2$Ag$_2$** along the b axis.
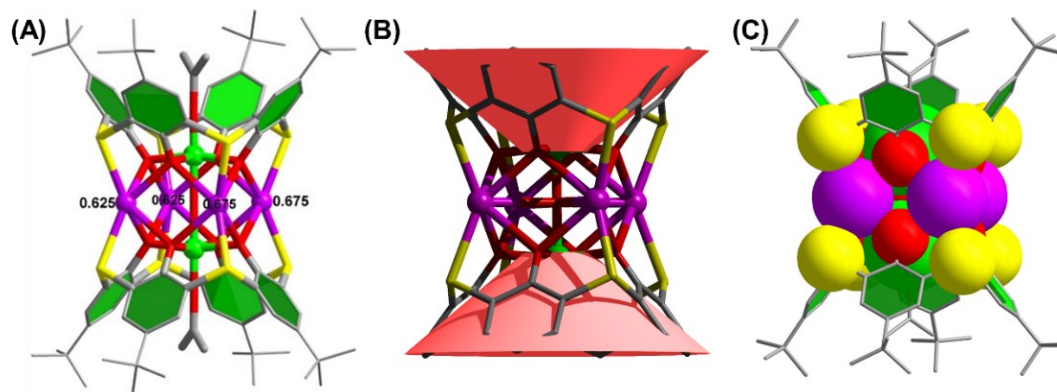
Figure S7. Molecular structures of **Ti$_2$Ag$_{2.6}$**. The four metal sites located between the two calixarenes are partially occupied by Ag$^+$ ions, with a total occupancy rate of 2.6 for the four Ag sites. EDX confirm that only Ag and Ti metals exist in the structure. ICP-AES for atomic ratios of Ag/Ti showed the Ag/Ti atomic ratio to be 1.3:1.
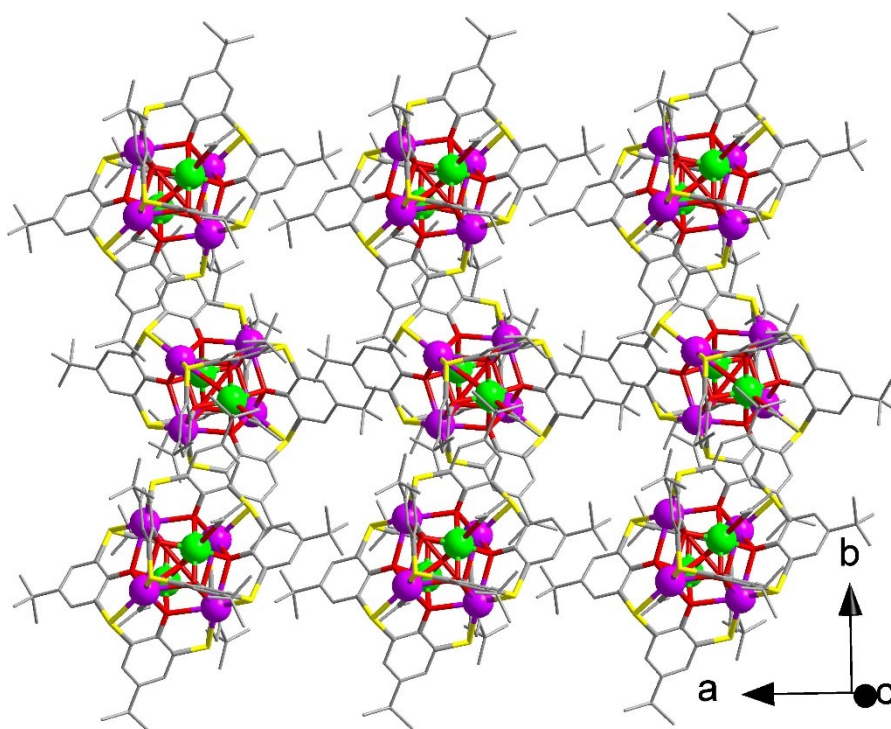
Figure S8. Three-dimensional packing structure of **Ti$_2$Ag$_{2.6}$** along the c axis.
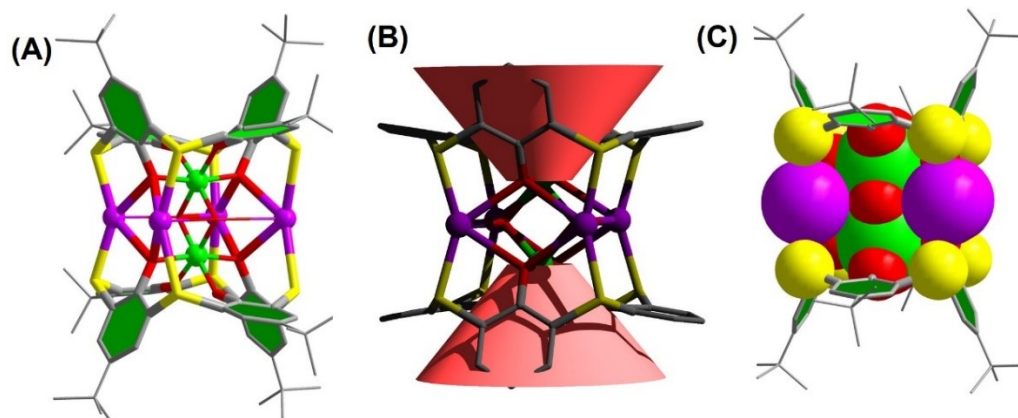
Figure S9. Molecular structures of **Ti$_2$Ag$_4$**.
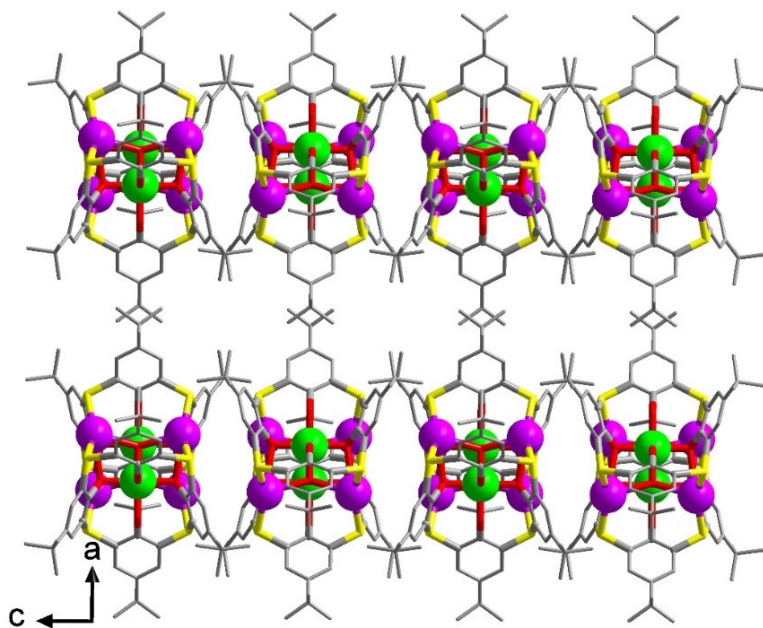
Figure S10. Three-dimensional packing structure of **Ti₂Ag₄** along the b axis.
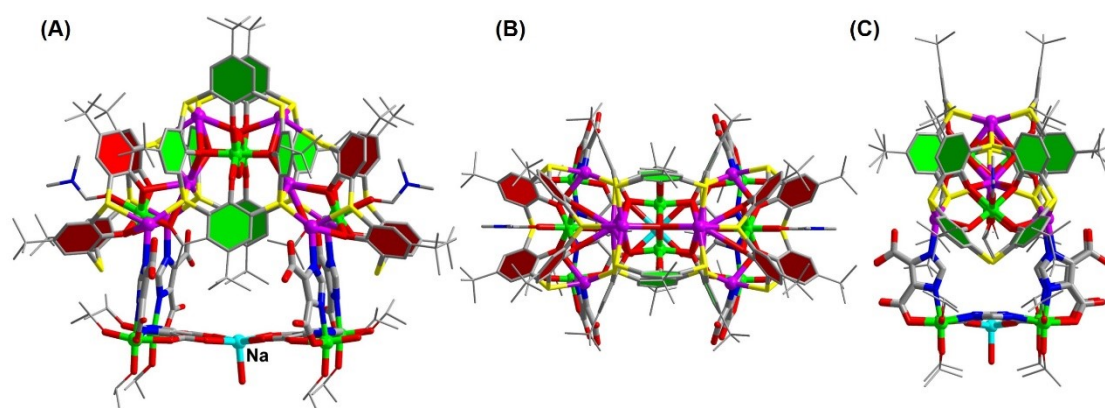
Figure S11. Molecular structures of **Ti₈Ag₈**.
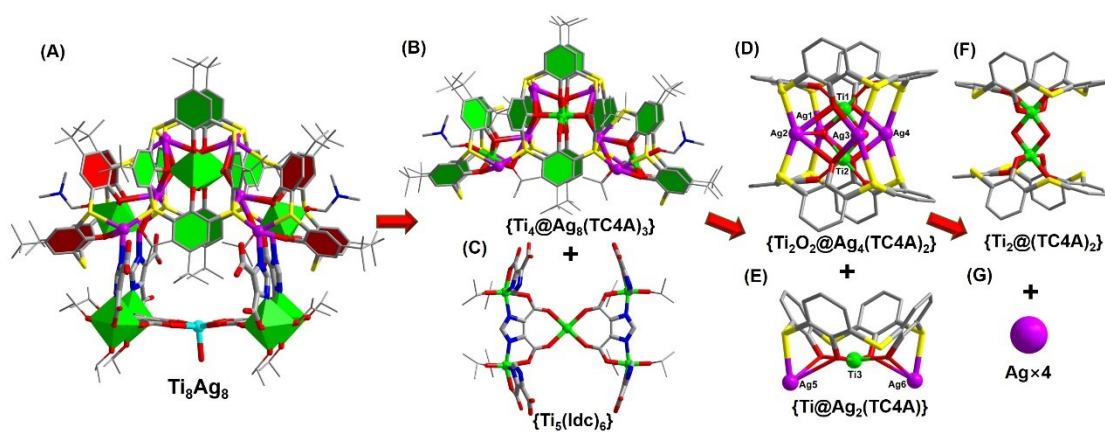
Figure S12. Molecular structures of **Ti₈Ag₈** under different viewing angles.
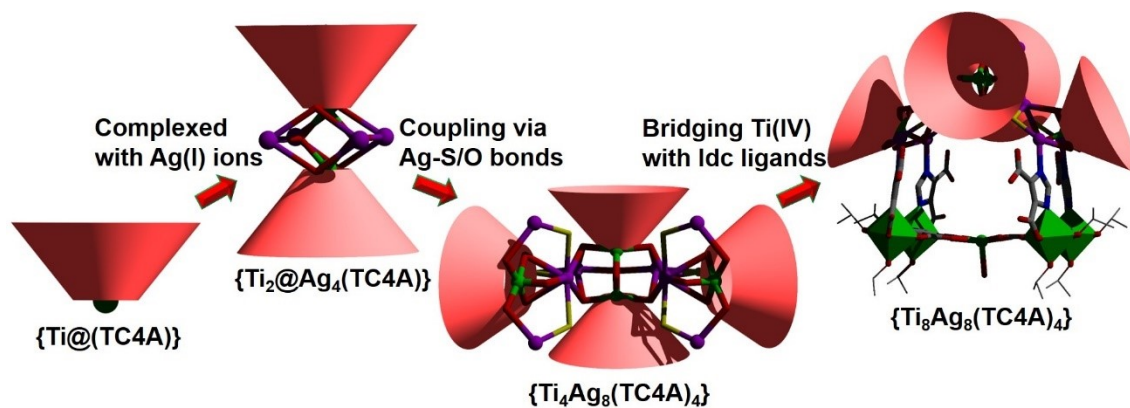
Figure S13. Stepwise assembly of thiacalix[4]arene-protected Ag/Ti bimetallic nanoclusters.

4. Powder X-ray diffraction
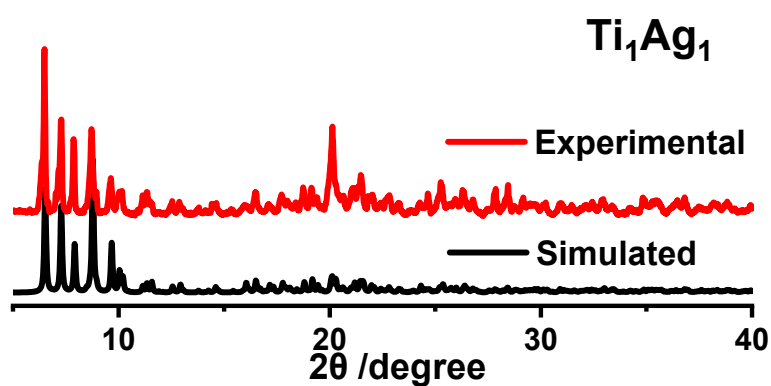
Figure S14. The XRD pattern of **Ti_1Ag_1.**
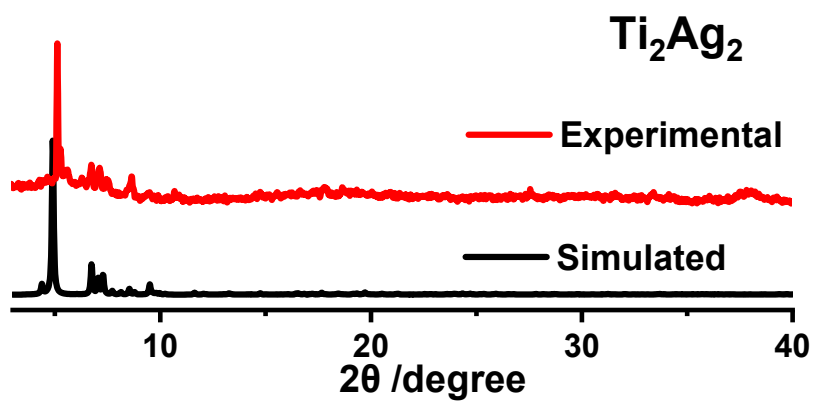
Figure S15. The XRD pattern of **Ti_2Ag_2.**
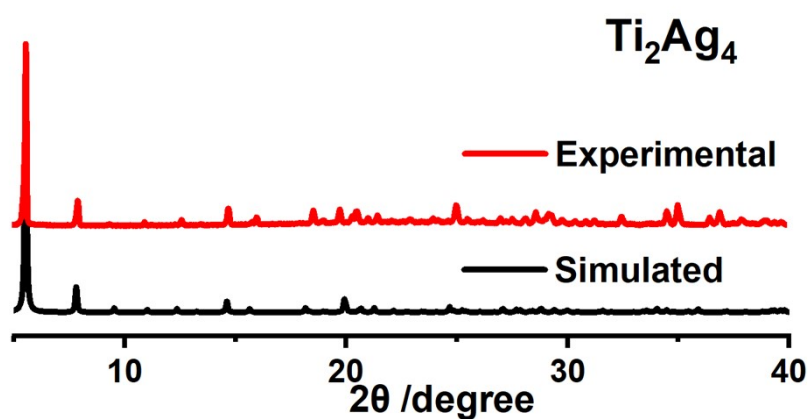
Figure S16. The XRD pattern of **Ti₂Ag₄**.
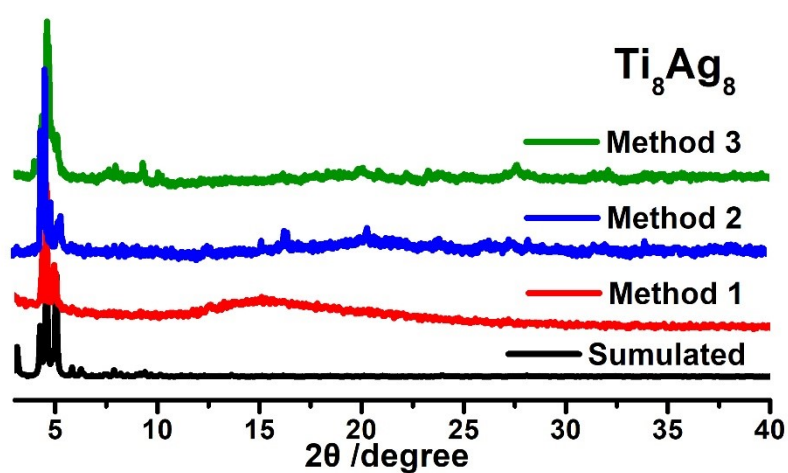
Figure S17. The XRD pattern of **Ti₈Ag₈**.

5. IR spectra
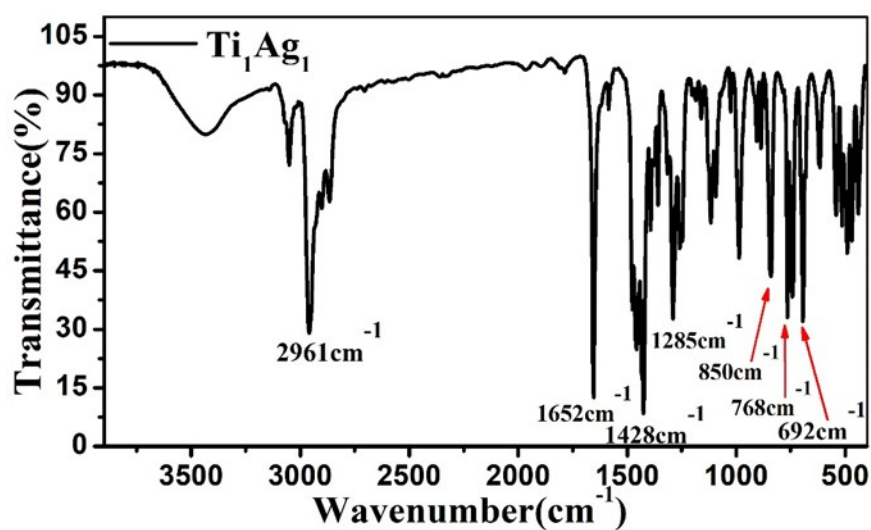
Figure S18. IR spectra of crystal sample of **Ti₁Ag₁**.
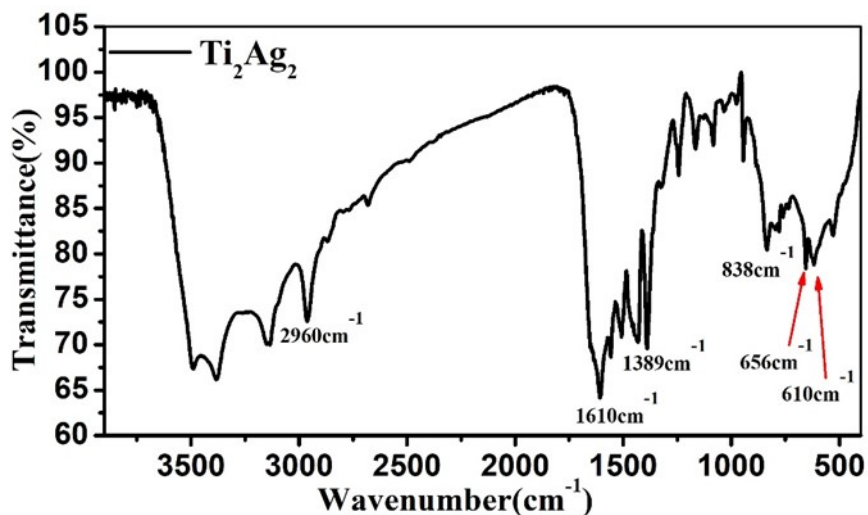
Figure S19. IR spectra of crystal sample of **Ti₂Ag₂**.
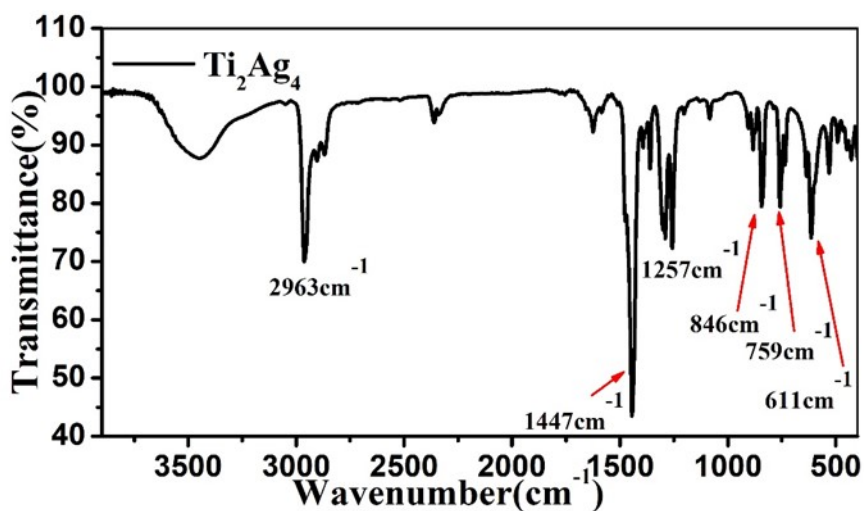
Figure S20. IR spectra of crystal sample of **Ti₂Ag₄**.
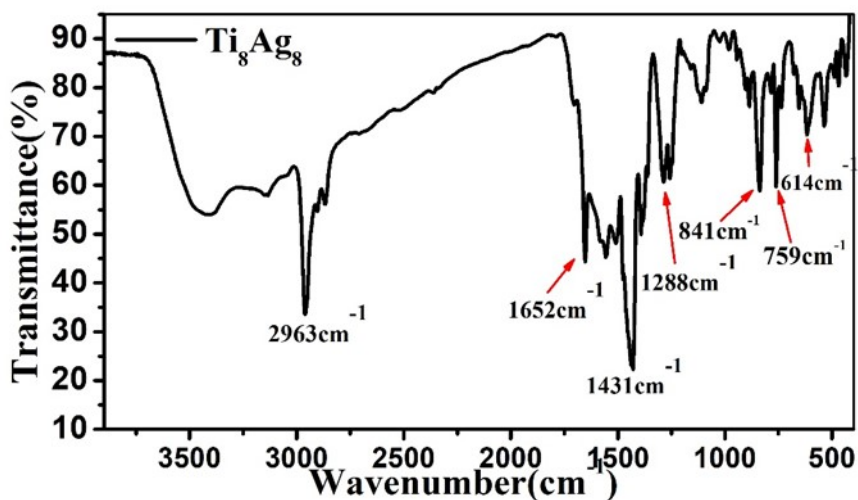
Figure S21. IR spectrum of crystal sample of **Ti₈Ag₈**.

6. TG-Measurement
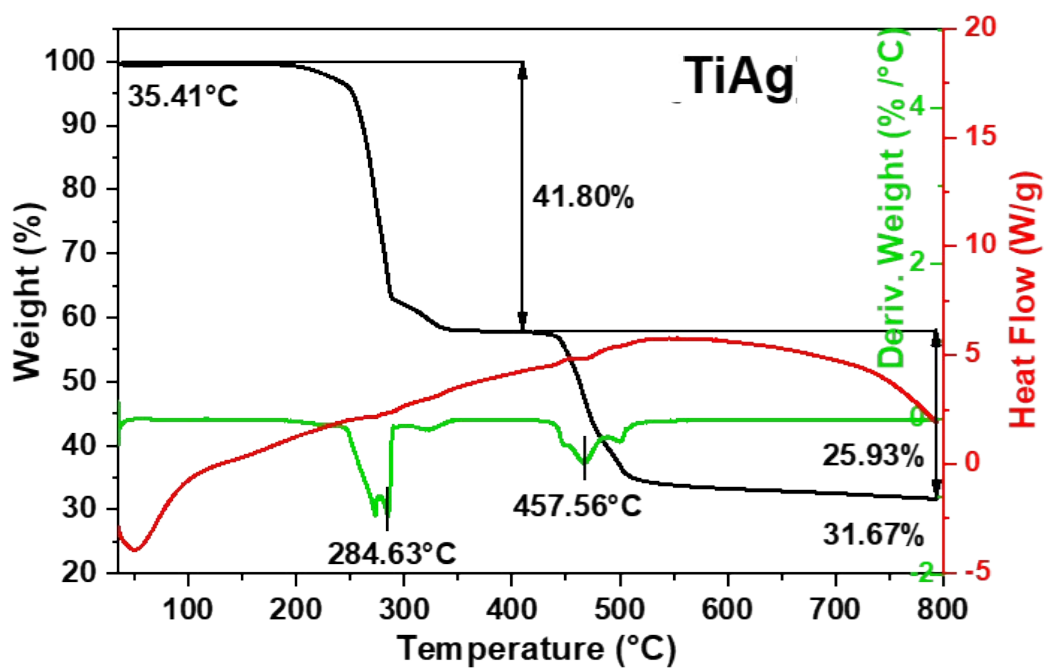
Figure S22. The TGA pattern of **Ti₁Ag₁**.
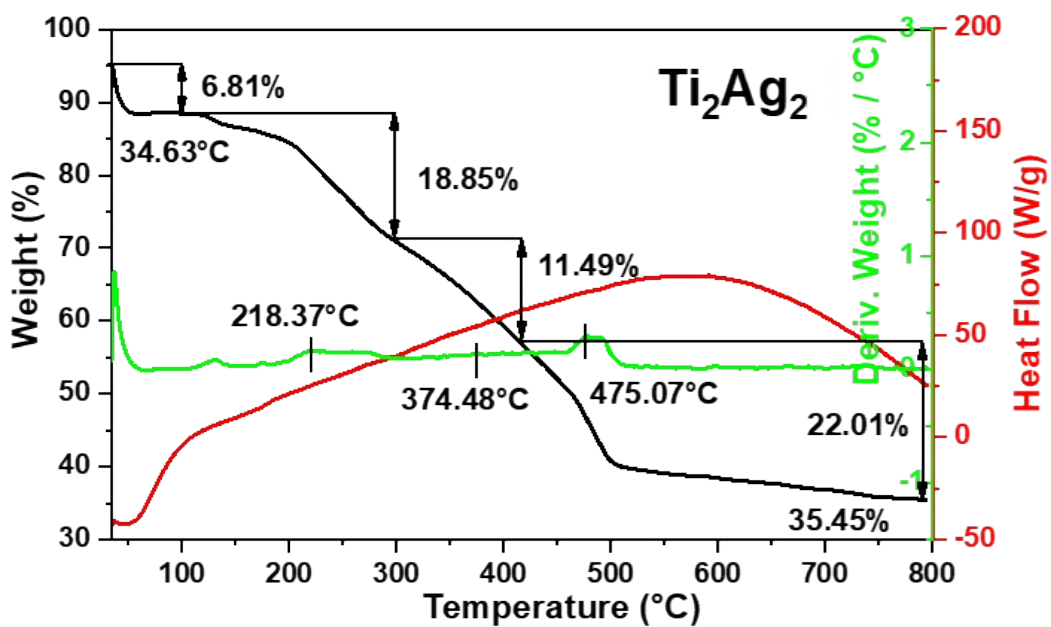
Figure S23. The TGA pattern of **Ti₂Ag₂**.
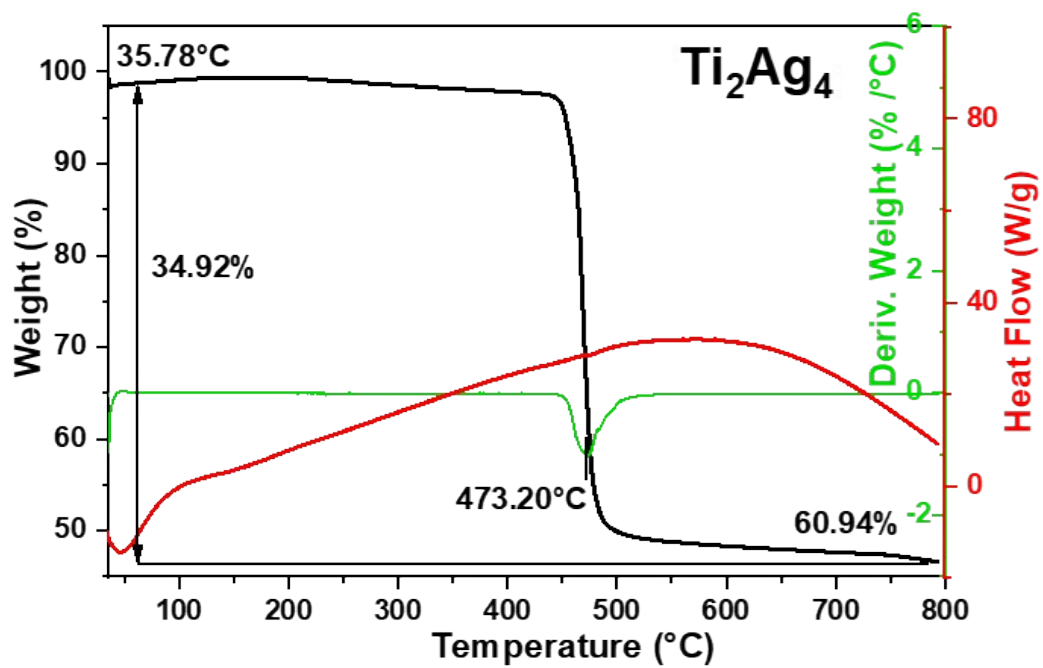
Figure S24. The TGA pattern of **Ti₂Ag₄**.
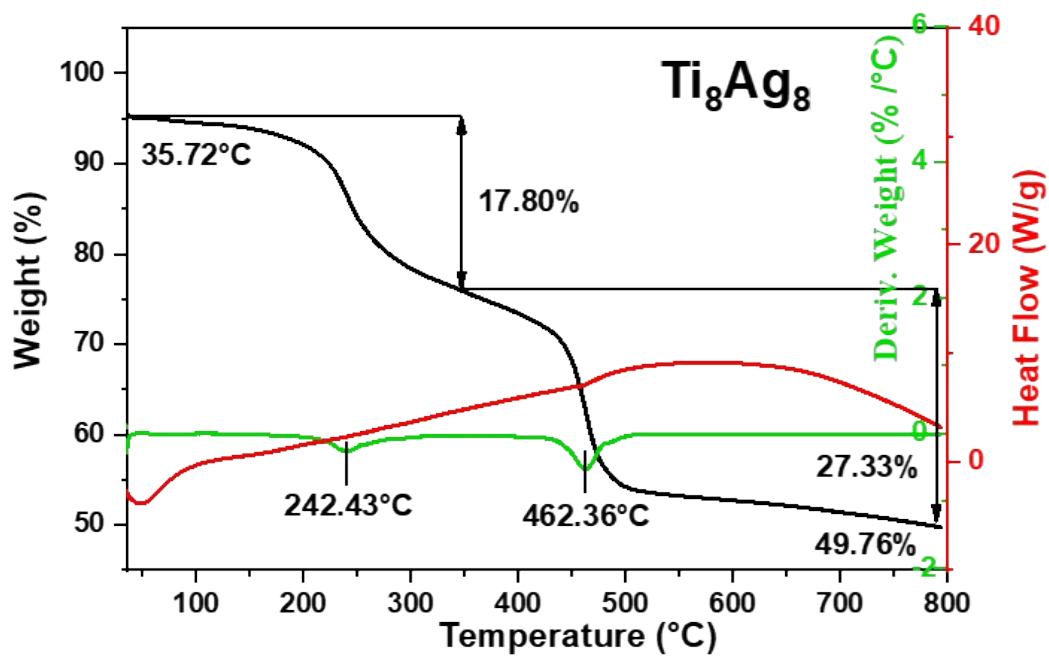
Figure S25. The TGA pattern of **Ti₈Ag₈**.

7. XPS analysis
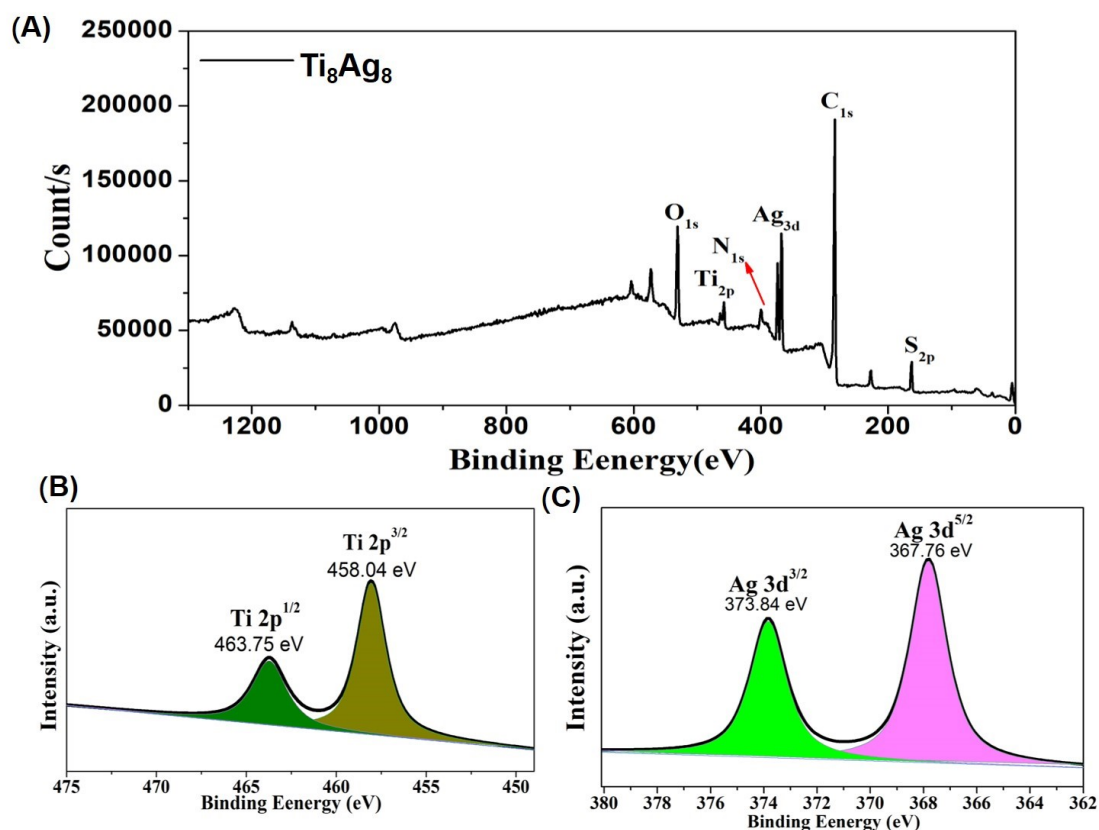
Figure S26. The XPS pattern of **Ti$_8$Ag$_8$.** The high-resolution Ti ^{2p} spectra for Ti$_8$Ag$_8$ clearly exhibit two regions of Ti 2p$^{1/2}$ and Ti 2p$^{3/2}$ with about 5.8 eV binding energy difference, being indicative of the sole presence of typical Ti^{4+}. Moving to the Ag region, the XPS peaks of **Ti$_8$Ag$_8$** are detected at 367.76 and 373.84 eV, consistent with the energy range of Ag 3d$^{5/2}$ and Ag 3d$^{3/2}$, respectively, thereby suggesting the presence of Ag in a +1-oxidation state
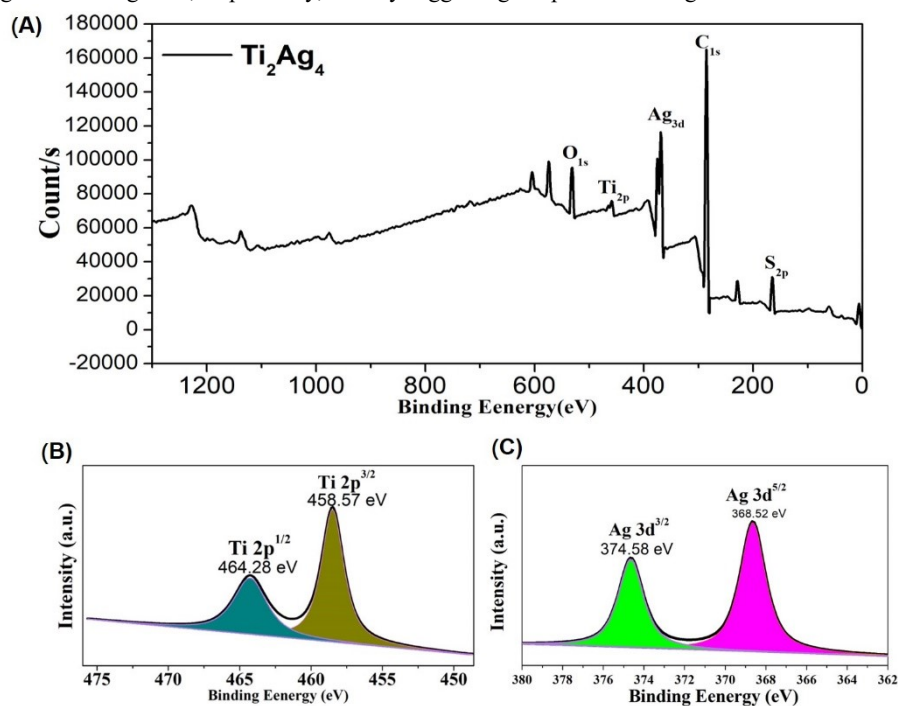
Figure S27. The XPS pattern of **Ti$_2$Ag$_4$.** The high-resolution Ti 2p spectra for Ti$_2$Ag$_4$ clearly exhibit two regions of Ti 2p$^{1/2}$ and Ti 2p$^{3/2}$ with about 5.7 eV binding energy difference, being indicative of the sole presence of typical Ti^{4+}. Moving to the Ag region, the XPS peaks of **Ti$_2$Ag$_4$** are detected at 368.52 and 374.58 eV, consistent with the energy range of Mo 3d5/2 and Mo 3d3/2, respectively, thereby suggesting the presence of Ag in a +1-oxidation state.

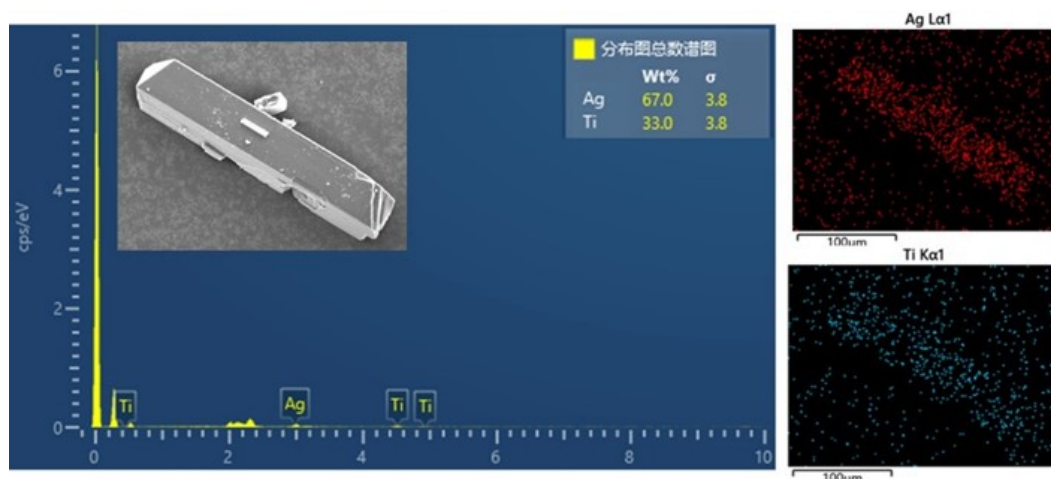## 8. Energy Dispersive X-ray (EDX) Spectroscopic Analysis
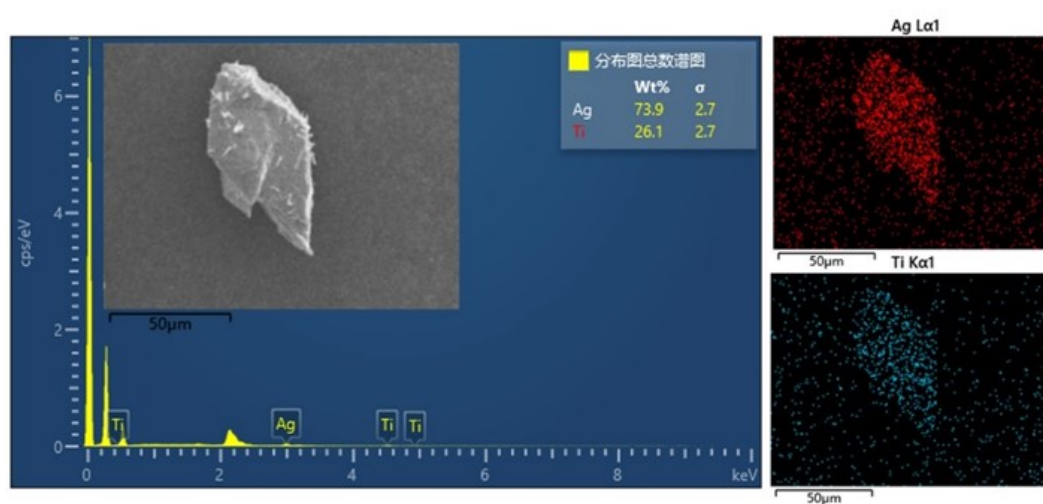

Figure S28. The EDS pattern of **Ti₁Ag₁.**

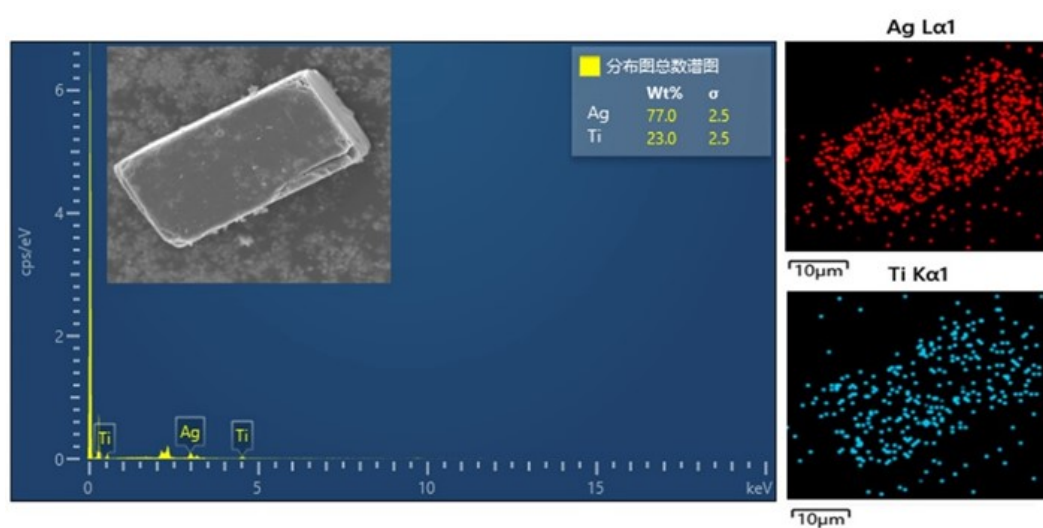**Figure S29.** The EDS pattern of **Ti₂Ag₂.**

Figure S30. The EDS pattern of **Ti₂Ag₄.**
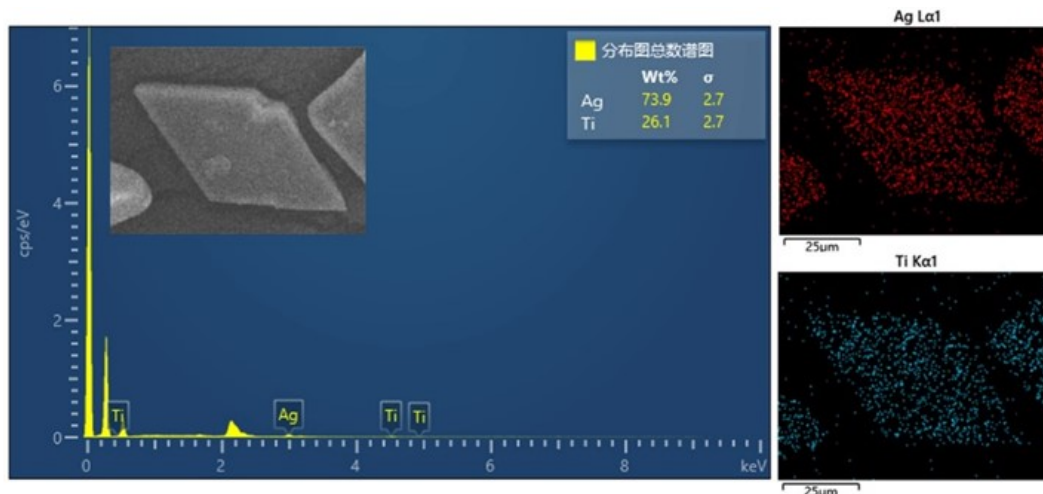
Figure S31. The EDS pattern of **Ti₈Ag₈.**

Table S2. ICP result of **Ti₈Ag₈.**

Element label	Weight (g)	Volume (ml)	Dilution coefficient	Instrument reading (mg/L)	Sample concentration(mg/kg)	Mass fraction%	Element ratio
Ti	0.0067	25	10	1.045303200	39003.9	3.9004%	7.85:7.95:1
Ag	0.0067	25	10	2.382808990	88910.8	8.8911%	
Na	0.0067	25	1	0.638758440	2383.4	0.2383%	

We have determined the atomic proportions of Ti:Ag:Na using the ICP method. The molar ratio of Ti:Ag:Na determined by ICP is 7.85:7.95:1, and the results are in good agreement with the theoretical values. In the synthesis of **Ti₈Ag₈**, we initially synthesized the compound through a reaction in a glass bottle. It is worth noting that glass bottles contain Na^+ ions, which can provide Na^+ ions during the reaction. To confirm this, we conducted further experiments using a 15ml teflon-lined stainless steel autoclave as the reaction vessel. Under the same reaction conditions, no **Ti₈Ag₈** crystals were formed. However, when we introduced Na_2SO_4 into the reaction as the Na^+ source, we were able to generate crystals of **Ti₈Ag₈** with higher yield and purity.
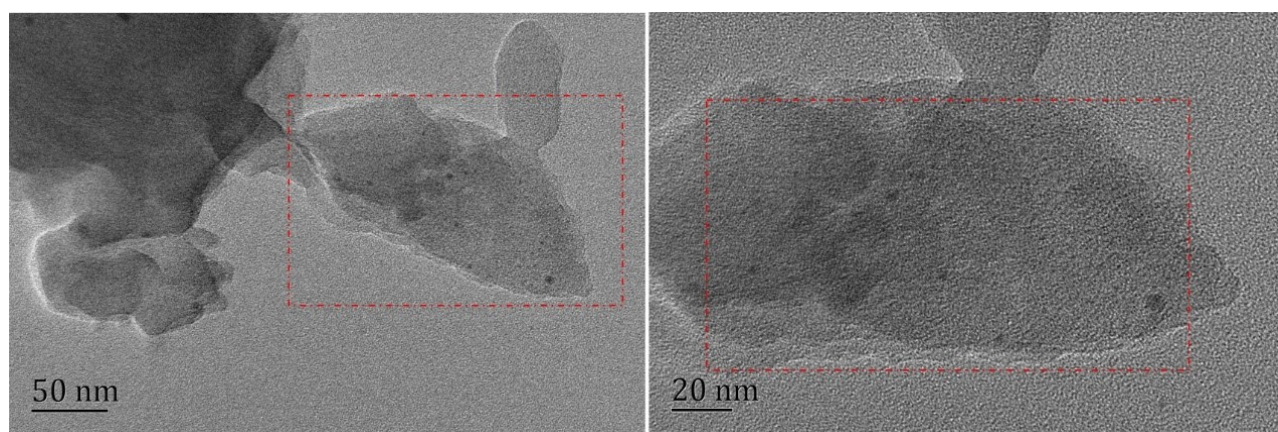

Figure S32. The TEM pattern of **Ti₈Ag₈.**

9. MS analysis

$[HTi_2Ag_2O(TC4A)_2]^{1+}$

$[H_3NaTi_8Ag_8O_2(TC4A)_4(Idc)_6(^iPrO)_4]^{2+}$

$[HTi_2Ag_6O_2(TC4A)_2(Idc)_2]^+$

$[HTi_2Ag_2O(TC4A)_2]^{1+}$
Found: m/z = 1762.13
Calcd: m/z= 1762.15

$[H_3NaTi_8Ag_8O_2(TC4A)_4(Idc)_6(^iPrO)_4]^{2+}$
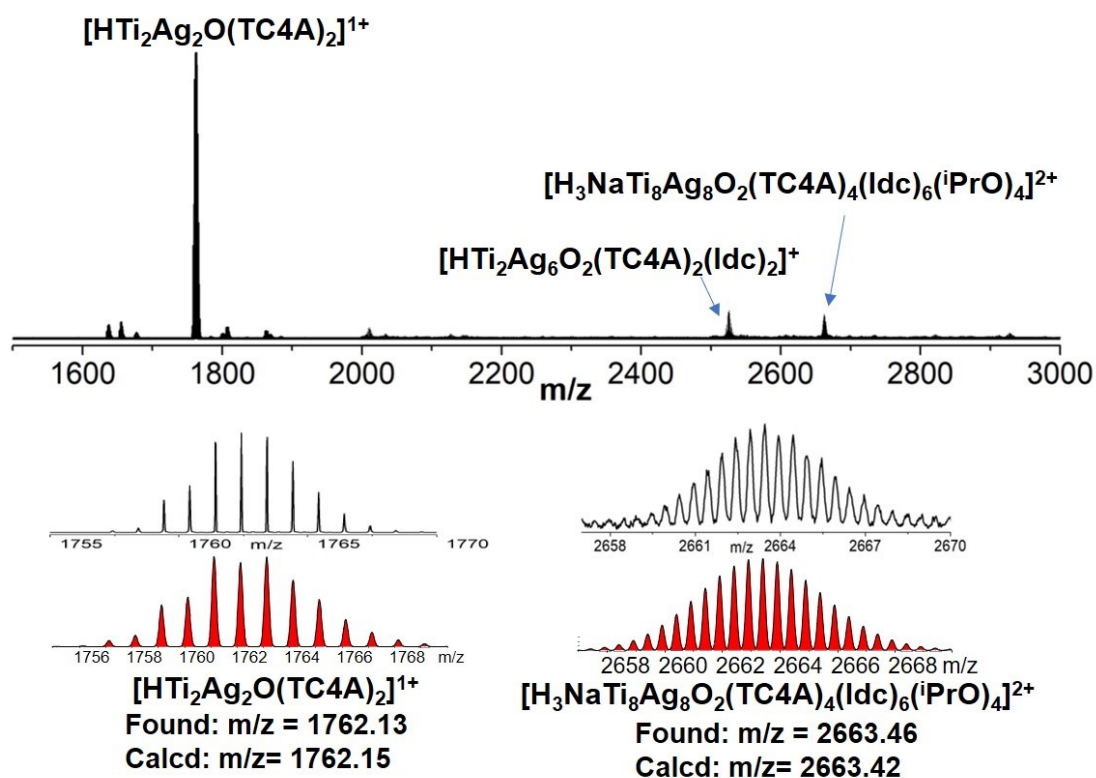Found: m/z = 2663.46
Calcd: m/z= 2663.42

Figure S33. Positive-ion mode ESI-MS of the crystals of **Ti$_8$Ag$_8$** dissolved in CH$_2$Cl$_2$. Zoom-in ESI-MS of experimental (black line) and simulated (red line) for specie.
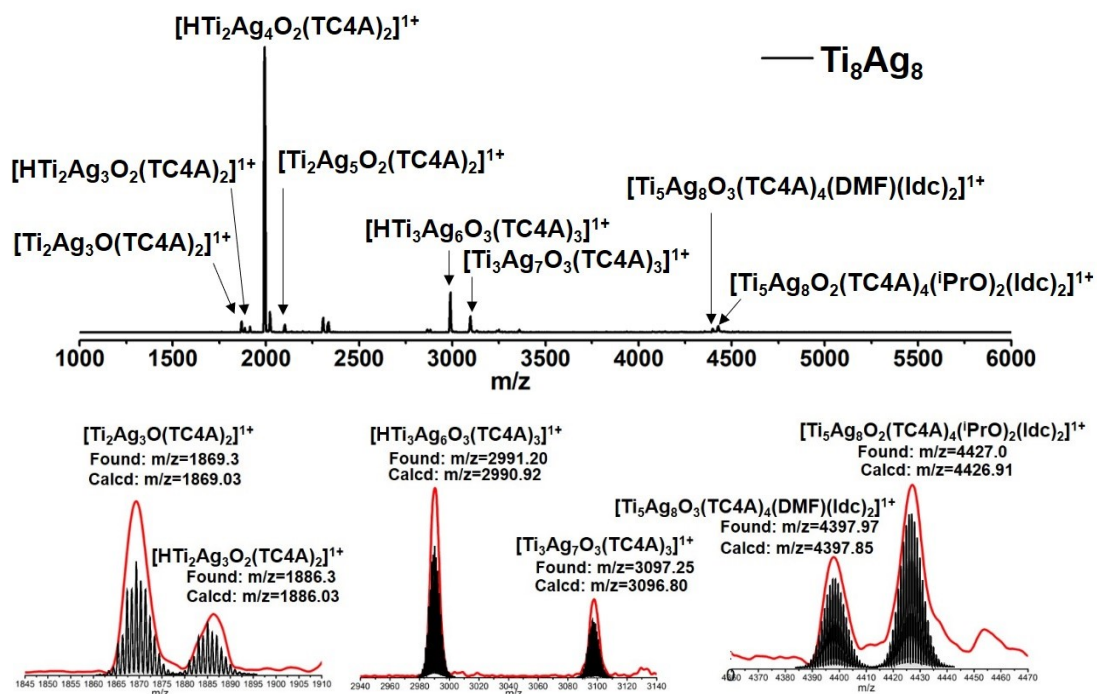

$[HTi_2Ag_4O_2(TC4A)_2]^{1+}$

— Ti$_8$Ag$_8$

$[HTi_2Ag_3O_2(TC4A)_2]^{1+}$

$[Ti_2Ag_5O_2(TC4A)_2]^{1+}$

$[Ti_5Ag_8O_3(TC4A)_4(DMF)(Idc)_2]^{1+}$

$[Ti_2Ag_3O(TC4A)_2]^{1+}$

$[HTi_3Ag_6O_3(TC4A)_3]^{1+}$

$[Ti_3Ag_7O_3(TC4A)_3]^{1+}$

$[Ti_5Ag_8O_2(TC4A)_4(^iPrO)_2(Idc)_2]^{1+}$

$[Ti_2Ag_3O(TC4A)_2]^{1+}$
Found: m/z=1869.3
Calcd: m/z=1869.03

$[HTi_3Ag_6O_3(TC4A)_3]^{1+}$
Found: m/z=2991.20
Calcd: m/z=2990.92

$[Ti_5Ag_8O_2(TC4A)_4(^iPrO)_2(Idc)_2]^{1+}$
Found: m/z=4427.0
Calcd: m/z=4426.91

$[Ti_5Ag_8O_3(TC4A)_4(DMF)(Idc)_2]^{1+}$
Found: m/z=4397.97
Calcd: m/z=4397.85

$[HTi_2Ag_3O_2(TC4A)_2]^{1+}$
Found: m/z=1886.3
Calcd: m/z=1886.03

$[Ti_3Ag_7O_3(TC4A)_3]^{1+}$
Found: m/z=3097.25
Calcd: m/z=3096.80

Figure S34. Positive-ion mode MALDI-TOF-MS of the crystals of **Ti$_8$Ag$_8$** dissolved in CH$_2$Cl$_2$. Zoom-in ESI-MS of experimental (black line) and simulated (red line) for specie.

Figure S35. Positive-ion mode MALDI-TOF-MS of the crystals of **Ti₂Ag₄** dissolved in CH₂Cl₂. Inset: Zoom-in ESI-MS of experimental (black line) and simulated (red line) for [HTi₂Ag₄O₂(TC4A)₂]¹⁺ specie.
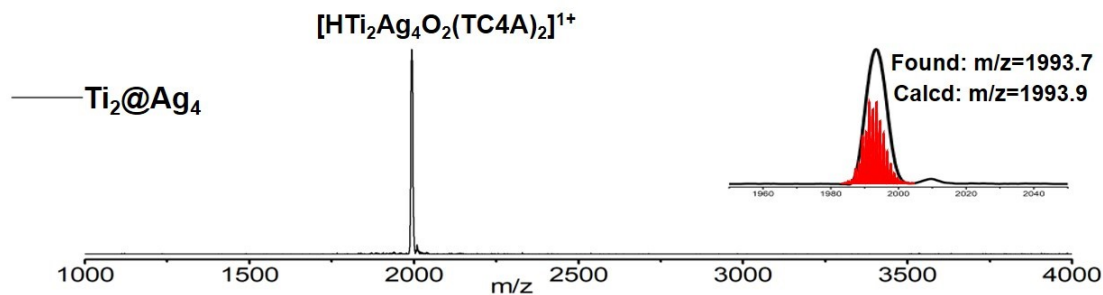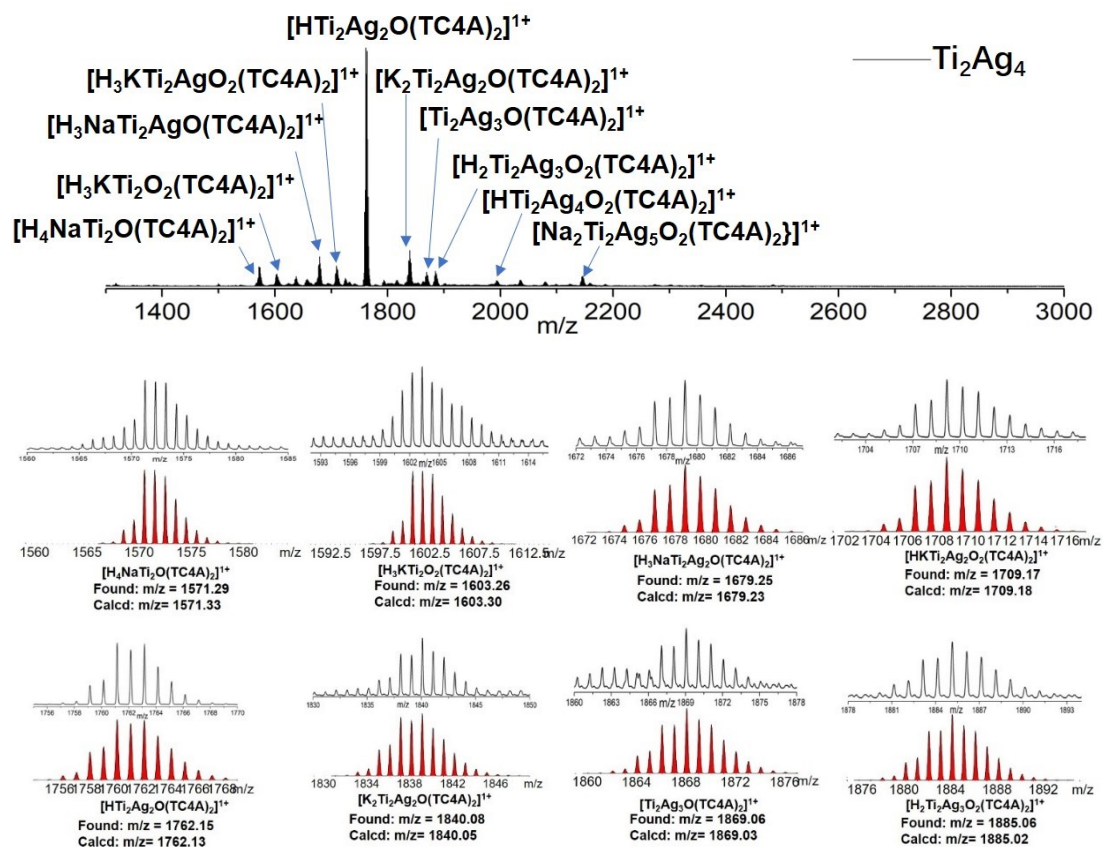

Figure S36. Positive-ion mode ESI-MS of the crystals of **Ti₂Ag₄** dissolved in CH₂Cl₂.

a: $[Ti_2Ag_x(TC4A)_2]^{1+}$

30 min

1 h

4 h

b: $\{[Ti_3Ag_8(TC4A)_3]\}^{1+}$

8 h

16 h

c: $\{[Ti_3Ag_8(TC4A)_4]\}^{1+}$

24 h

d: $\{[Ti_6Ag_8(TC4A)_4]\}^{2+}$

48 h

e: $\{[Ti_8Ag_8(TC4A)_4]\}^{2+}$

b: [H₃NaTi₃Ag₈O₂(TC4A)₃(Idc)(ⁱPrO)₂(DMF)₂]⁺
Found: m/z = 3633.70
Calcd: m/z= 3633.93

c: [HTi₄Ag₈O₂(TC4A)₃(Idc)(OH)₂(DMF)₂]⁺
Found: m/z = 3988.76
Calcd: m/z= 3988.78

d: [H₃NaTi₆Ag₈O₂(TC4A)₄(HIdc)₅(ⁱPrO)₃]²⁺
Found: m/z = 2500.30
Calcd: m/z= 2500.47
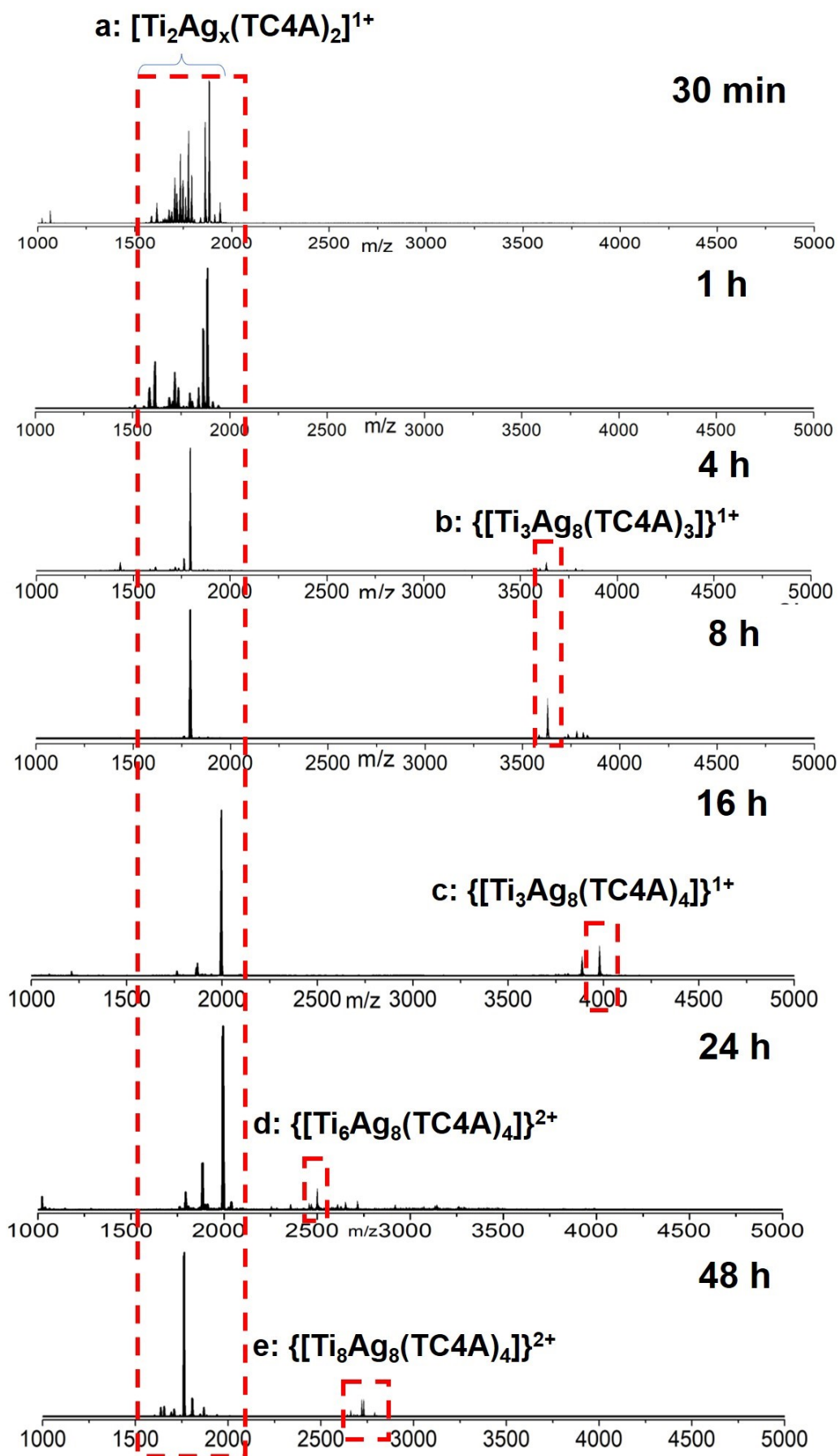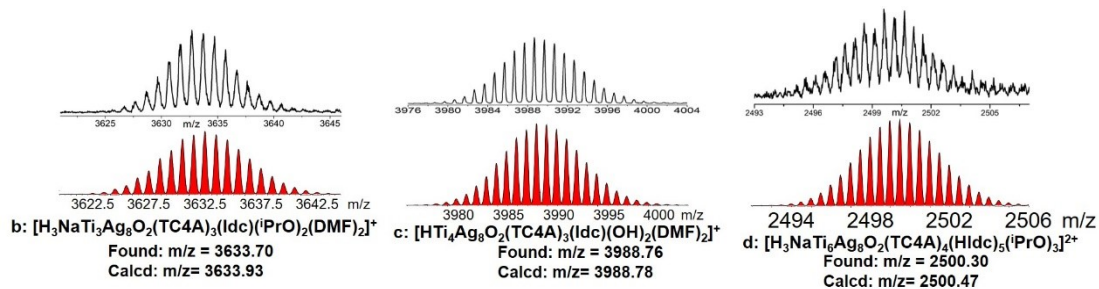
Figure S37. Time-dependent ESI-MS in range of m/z 1000 – 5000 on the reaction of f **Ti₂Ag₄**, Ti(OⁱPr)₄ and IdcH2 in ⁱPrOH/DMF at 80℃ at 1 h, 4h, 8h, 16h, 24 h and 48 h.

[Ti₂Ag(TC4A)₂]¹⁺
Found: m/z = 1637.24
Calcd: m/z= 1637.22

[H₂Ti₂AgO(TC4A)₂]¹⁺
Found: m/z = 1655.22
Calcd: m/z= 1655.24

[HKTi₂AgO(TC4A)₂]¹⁺
Found: m/z = 1693.18
Calcd: m/z= 1693.19

[HKTi₂AgO₂(TC4A)₂]¹⁺
Found: m/z = 1709.17
Calcd: m/z= 1709.18

[HTi₂Ag₂O(TC4A)₂]¹⁺
Found: m/z = 1662.14
Calcd: m/z= 1762.13

[Na₂Ti₂Ag₂O(TC4A)₂]¹⁺
Found: m/z = 1807.14
Calcd: m/z= 1807.10

[Ti₂Ag₃O(TC4A)₂]¹⁺
Found: m/z = 1869.02
Calcd: m/z= 1869.03
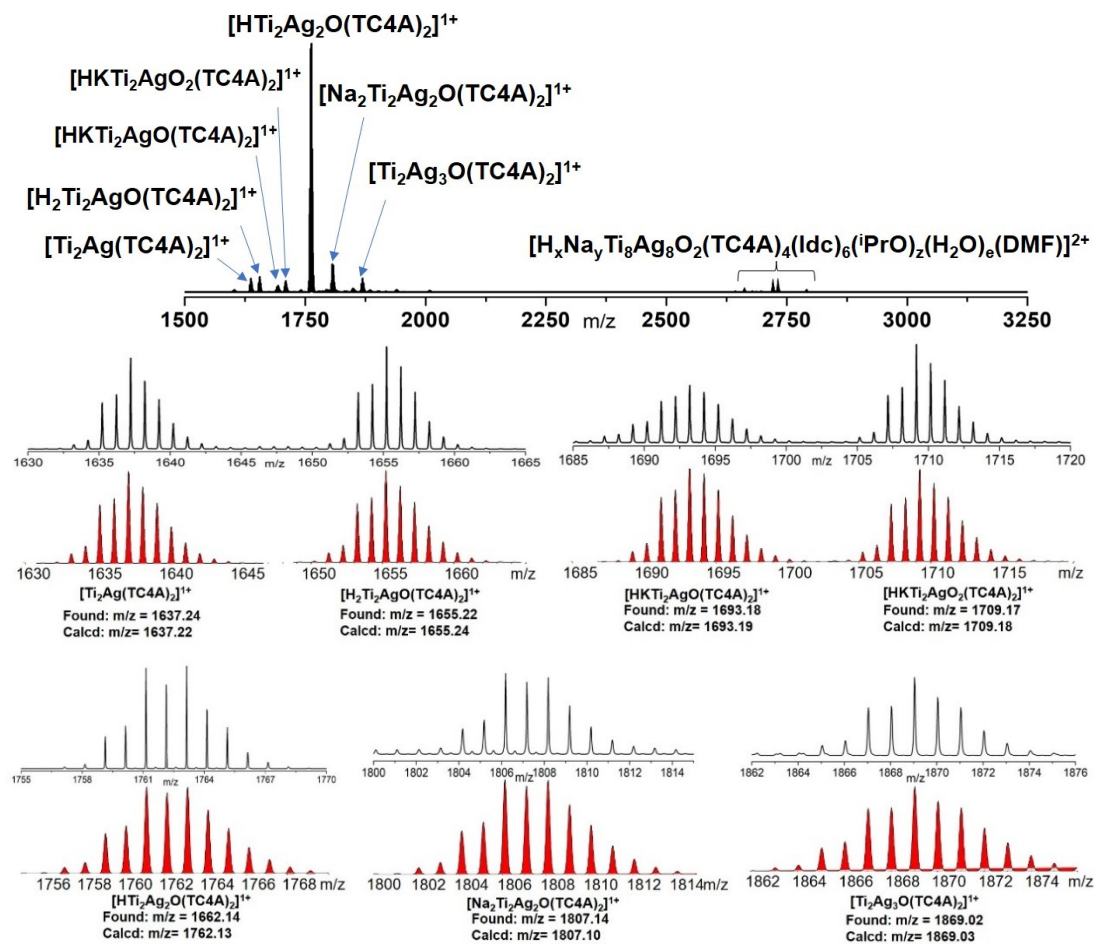
Figure S38. Positive-ion mode ESI-MS of the mother liquor of **Ti₂Ag₄**, Ti(OⁱPr)₄ and IdcH₂ in ⁱPrOH/DMF at 80℃ after 48 hour.
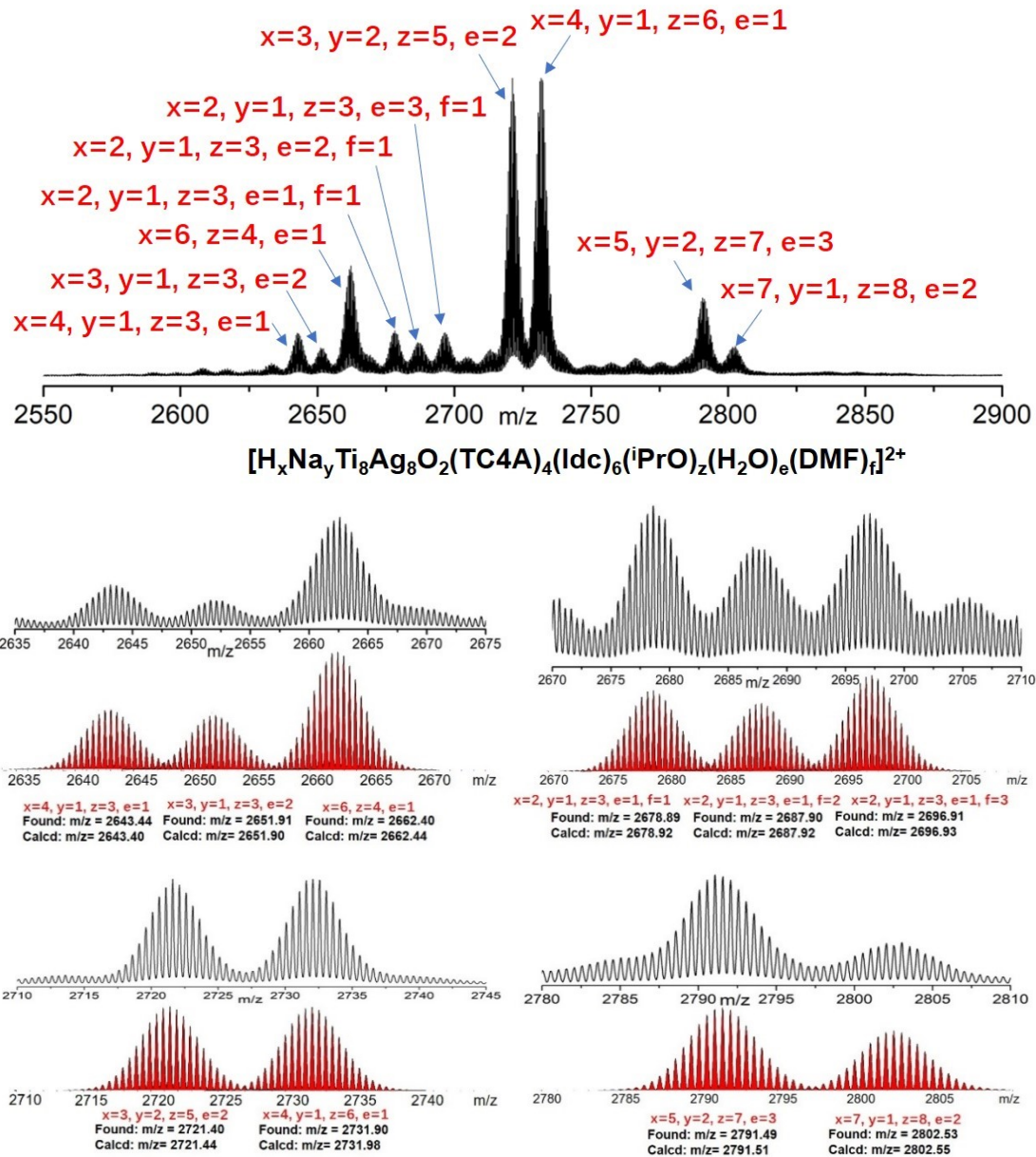
Figure S39. ESI-MS of experimental and simulated for $[H_xNa_yTi_8Ag_8O_2(TC4A)_4(Idc)_6(^iPrO)_z(H_2O)_e(DMF)_f]^{2+}$.

10. Electrocatalytic CO$_2$ Reduction
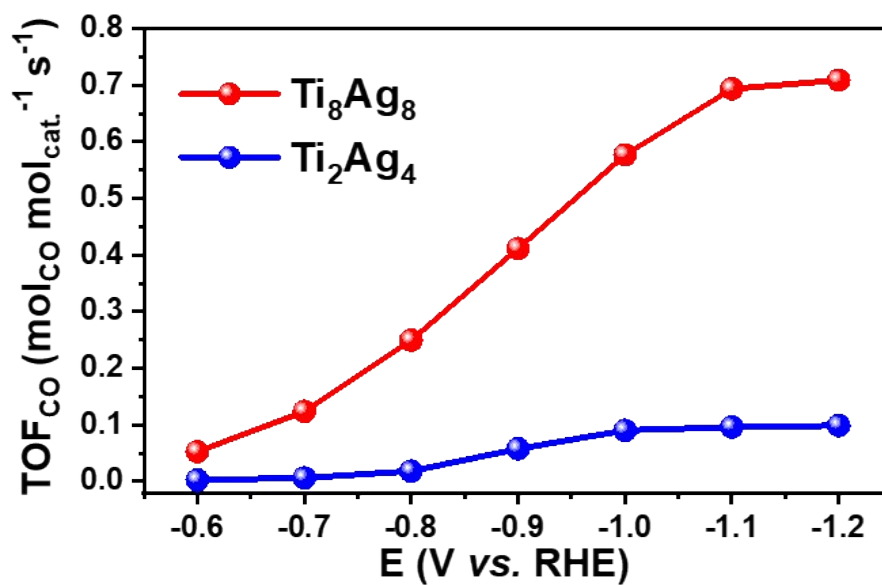
Figure S40. CO$_2$RR turnover frequencies (TOF) of **Ti$_2$Ag$_4$** and **Ti$_8$Ag$_8$**.
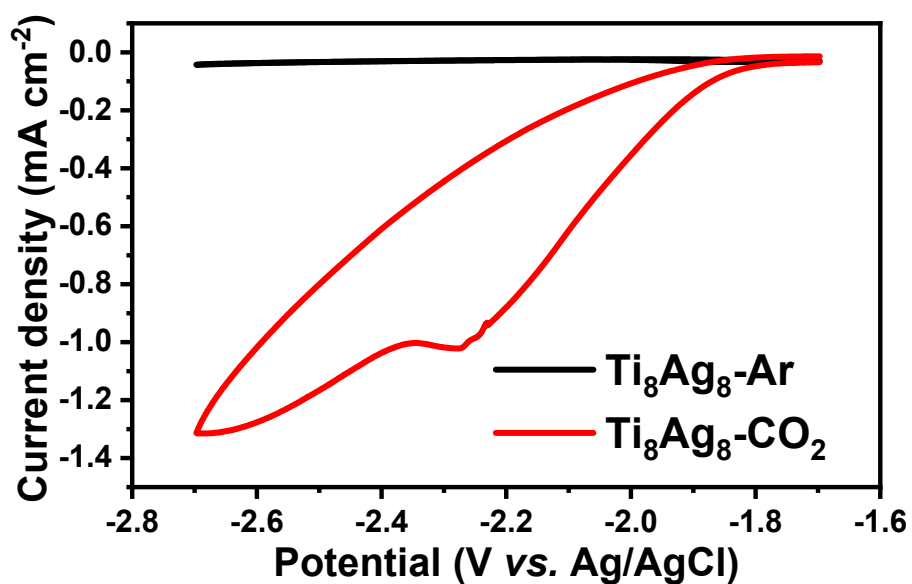
Figure 41. Cyclic voltammetry of **Ti$_8$Ag$_8$** in CO$_2$ and Ar-saturated 0.1 M anhydrous acetronitrile solution of tetrbutyl ammonium bromide.
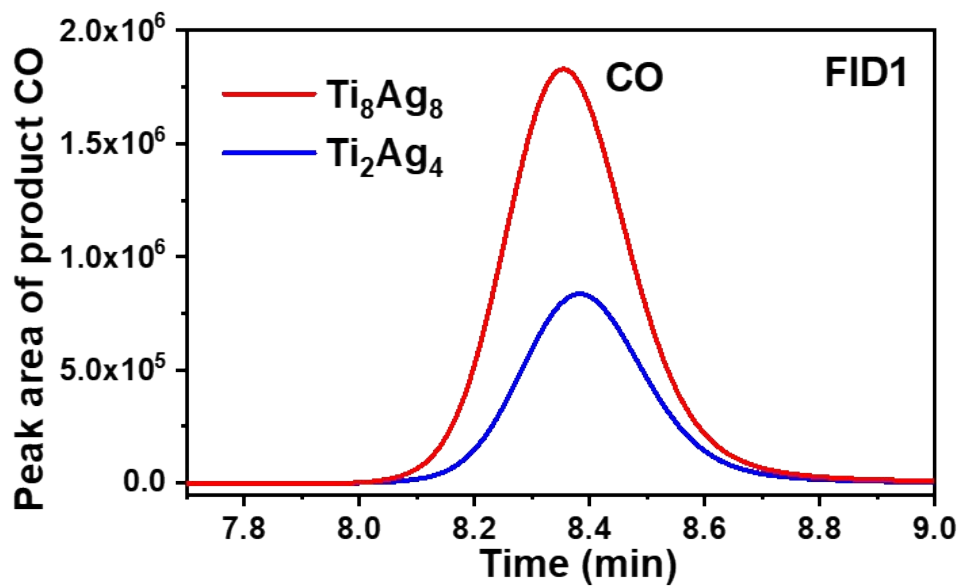
Figure S42. Gas chromatography of product (CO). The gas (CO) was detected and analyzed by GC (GC-2014C) equipped with two flame ionization detector (FID1 and FID2) and a thermal conductivity (TCD). Among them, FID1 was used to analyze CO.
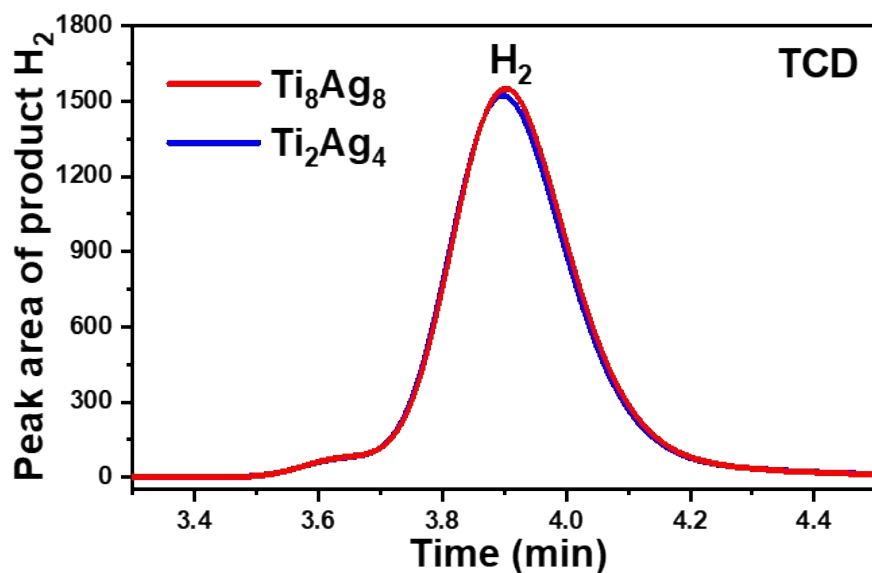
Figure S43. Gas chromatography of product (H_2). The gas (H_2) was detected and analyzed by GC (GC-2014C) equipped with two flame ionization detector (FID1 and FID2) and a thermal conductivity (TCD). Among them, TCD was used to analyze H_2.
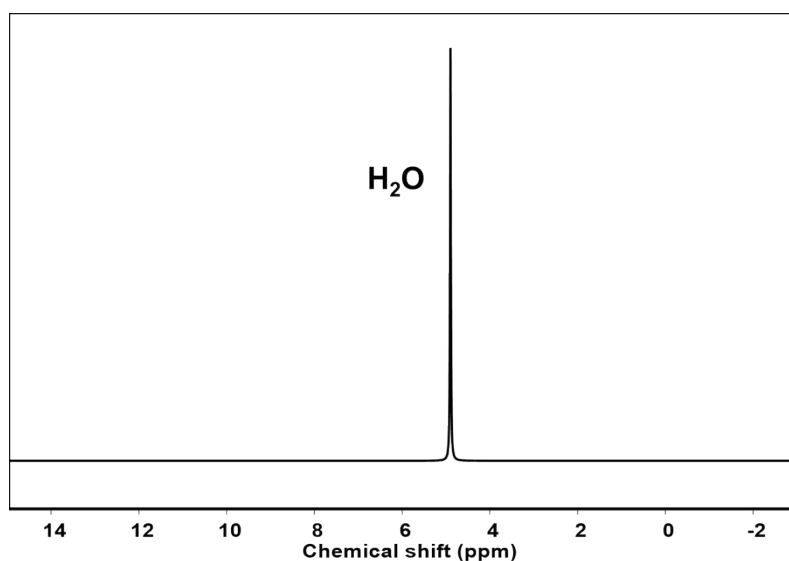
Figure S44. Characterization for the liquid product of **Ti₈Ag₈** during CO_2 reduction process by ^1H nuclear magnetic resonance spectroscopy. There are only H_2O peak in the figure, indicating that there is no product in the liquid phase.
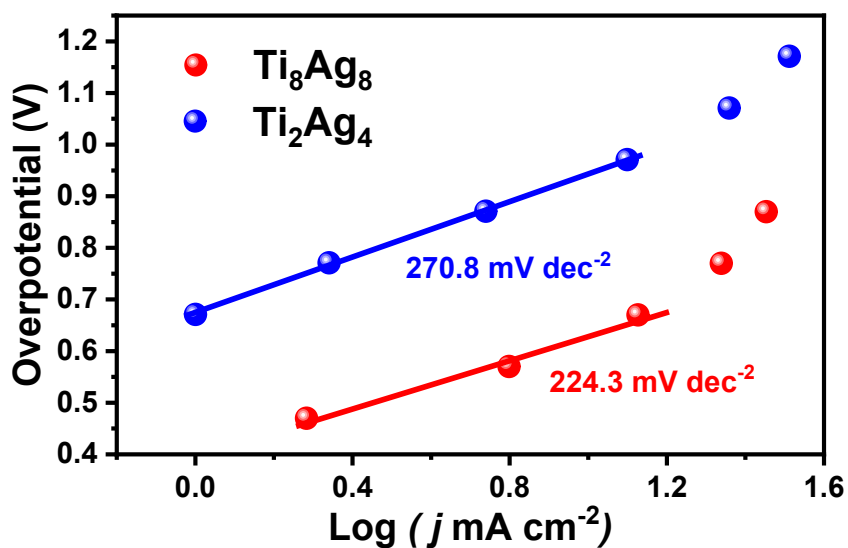
Figure S45. Tafel plots of **Ti₈Ag₈** and **Ti₂Ag₄**.
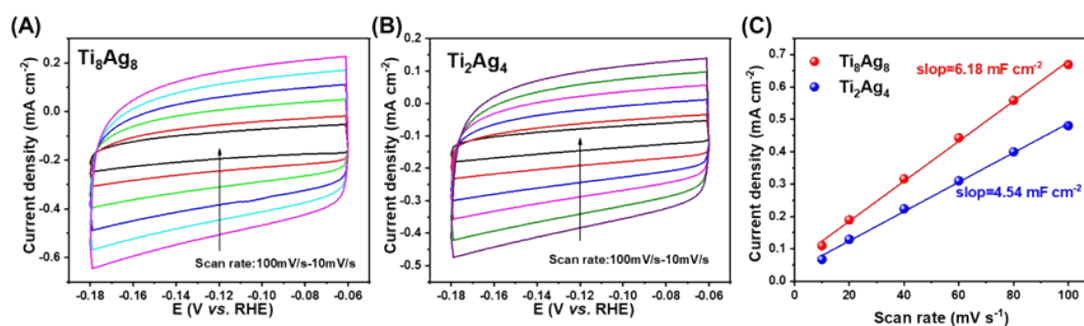
Figure S46. Cyclic voltammertrys (CV) curves in the region of -0.18 ~-0.06 V vs. RHE at various scan rate (10 ~ 100 mV s⁻¹) and corresponding capacitive current at -0.12 V as a function of scan rate for (a) **Ti₈Ag₈**. (b) **Ti₂Ag₄**. (c) Electrochemical active surface area (ECSA) measurement was estimated by CV at different scan rates from 10 to 100 mV s⁻¹ under the potential window of -0.18 V to -0.06 V (vs. RHE) to measure the double-layer capacitance (C_{dl}).
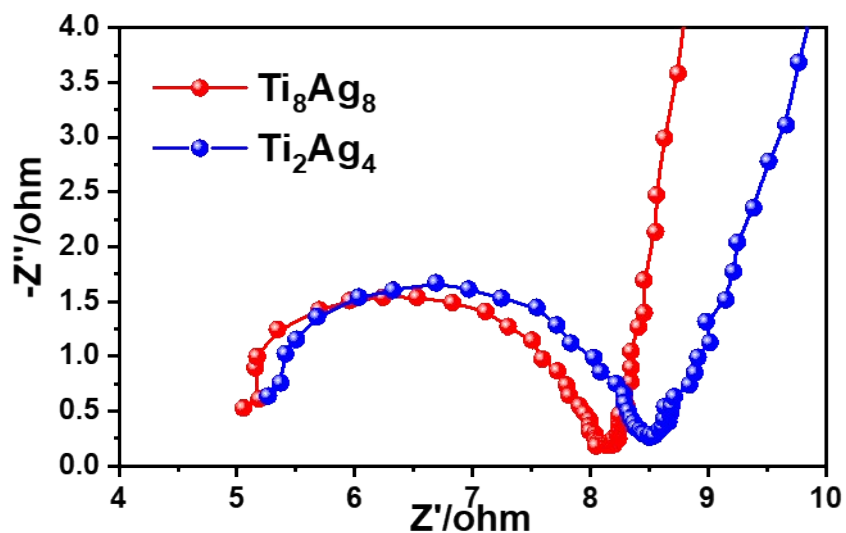
Figure S47. Nyquist plots of electrocatalysts over the frequency ranging from 100 kHz to 10mHz at −0.9 V vs. RHE.
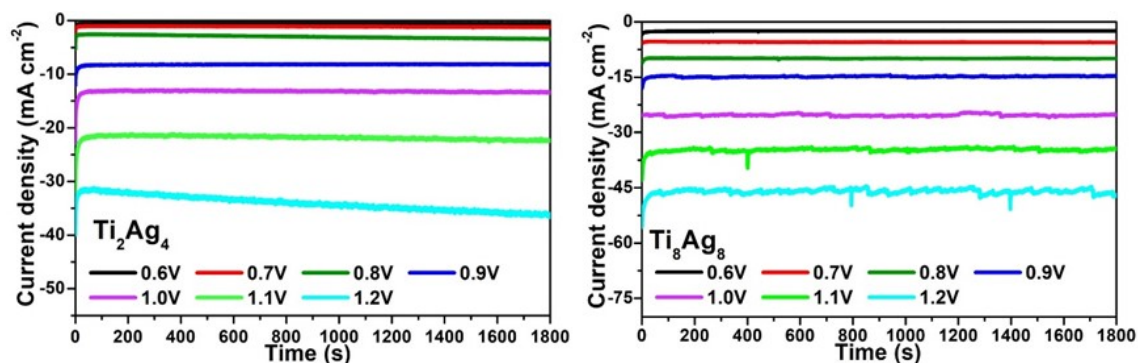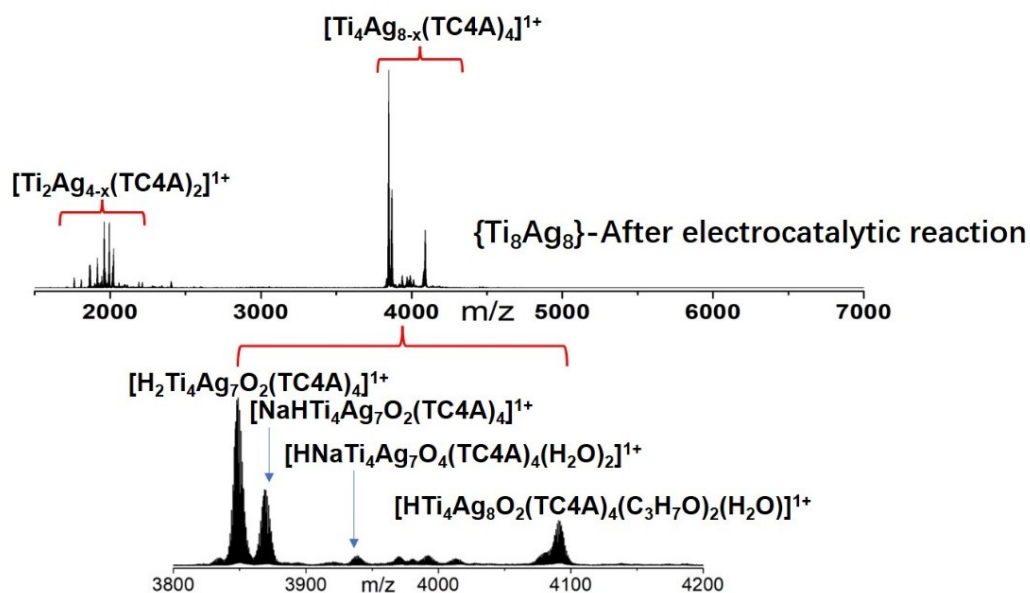

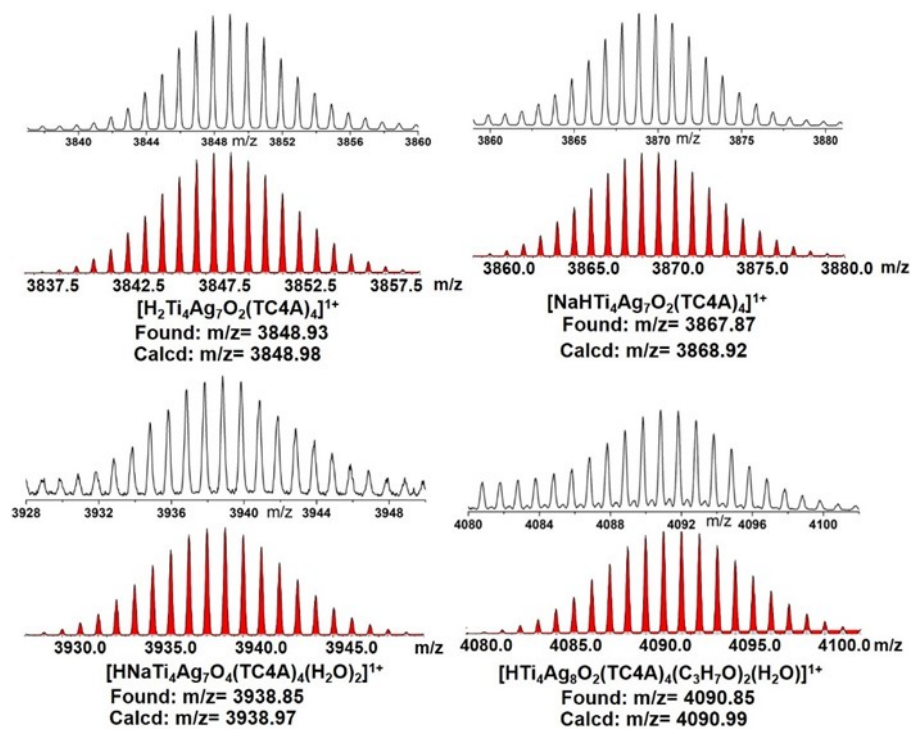**Figure S48.** i-t curve of catalyst at different fixed voltage.

Figure S49. Positive-ion mode ESI-MS of the **Ti₈Ag₈** sample after reaction dissolved in CH₂Cl₂.
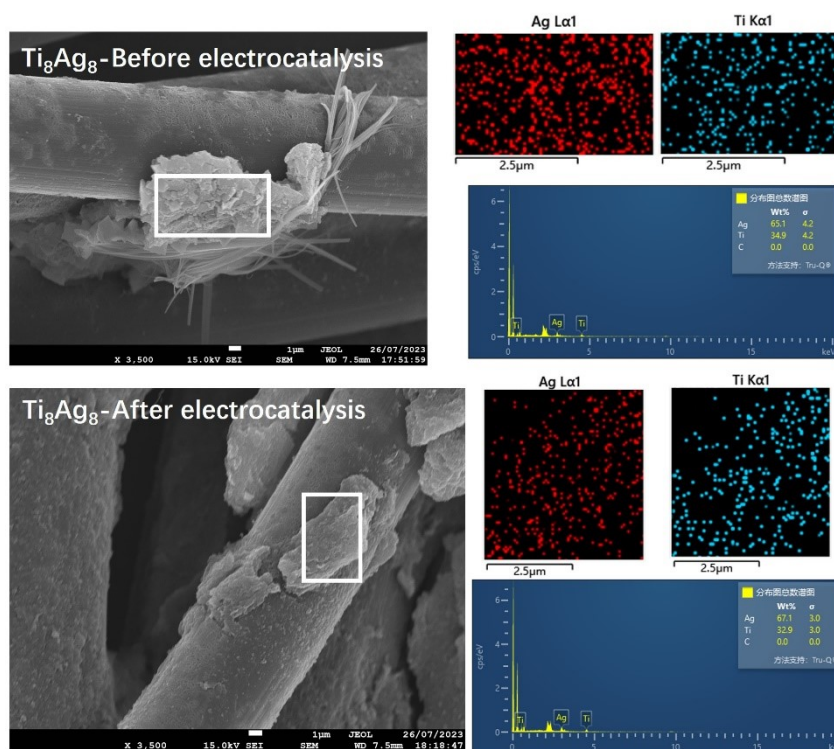

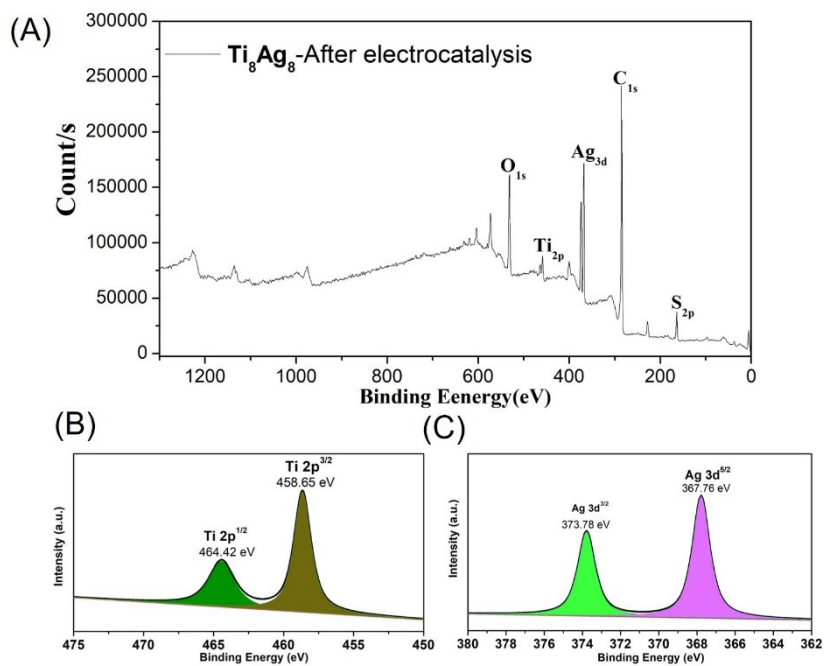**Figure S50**. EDS of **Ti₈Ag₈** after catalysis tests.

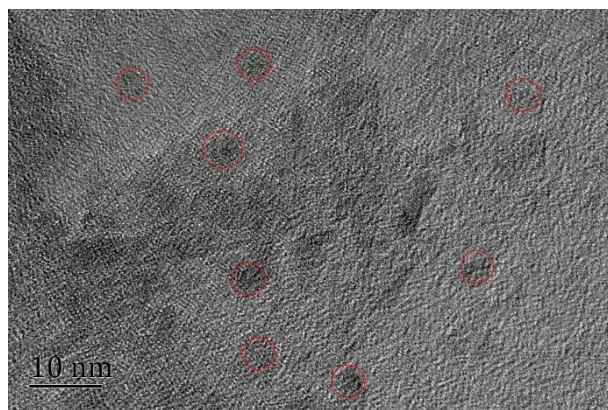**Figure S51.** XPS of **Ti₈Ag₈** after catalysis tests.

Figure S52. TEM micrograph of **Ti₈Ag₈** after catalysis tests.

11. Computational Detail

d-band center (ε_d)
Ag1=Ag2=Ag7=Ag8 = -0.34
Ag3=Ag4 = -0.40
Ag5=Ag6 = -0.51

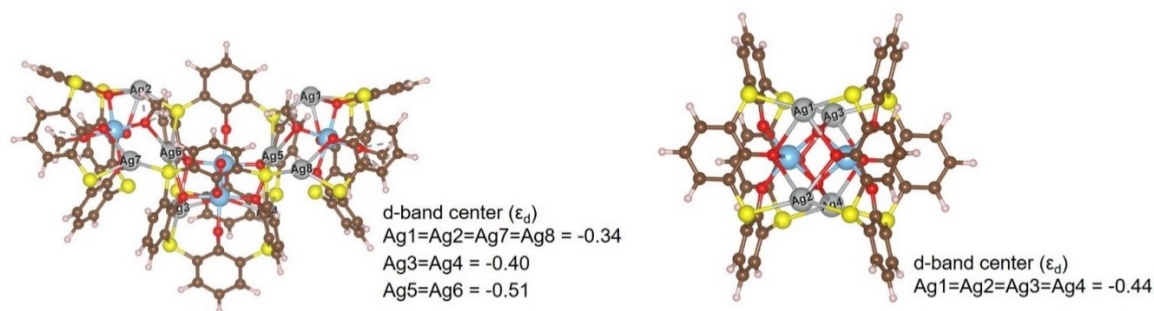d-band center (ε_d)
Ag1=Ag2=Ag3=Ag4 = -0.44

Figure S53. Positive-ion mode ESI-MS of the **Ti₈Ag₈** sample after reaction dissolved in CH_2Cl_2.
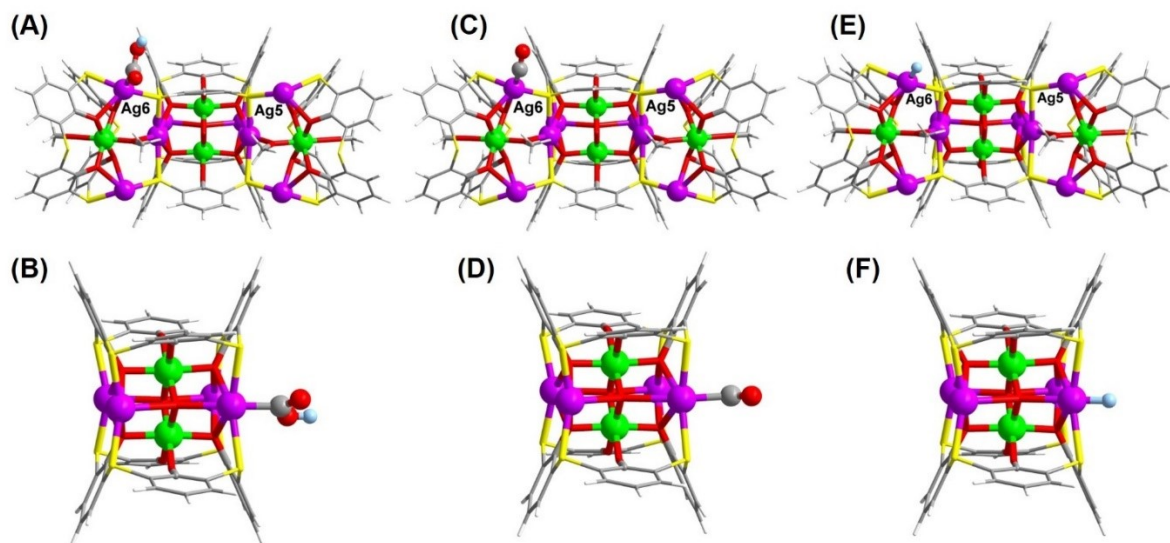
Figure S54. The calculation optimized structures of COOH absorbed on **Ti₄Ag₈_m** (A) and **Ti₂Ag₄_m** (B); The calculation optimized structures of CO absorbed on **Ti₄Ag₈_m** (C) and **Ti₂Ag₄_m** (D); The calculation optimized structures of H absorbed on **Ti₄Ag₈_m** (E) and **Ti₂Ag₄_m** (F).
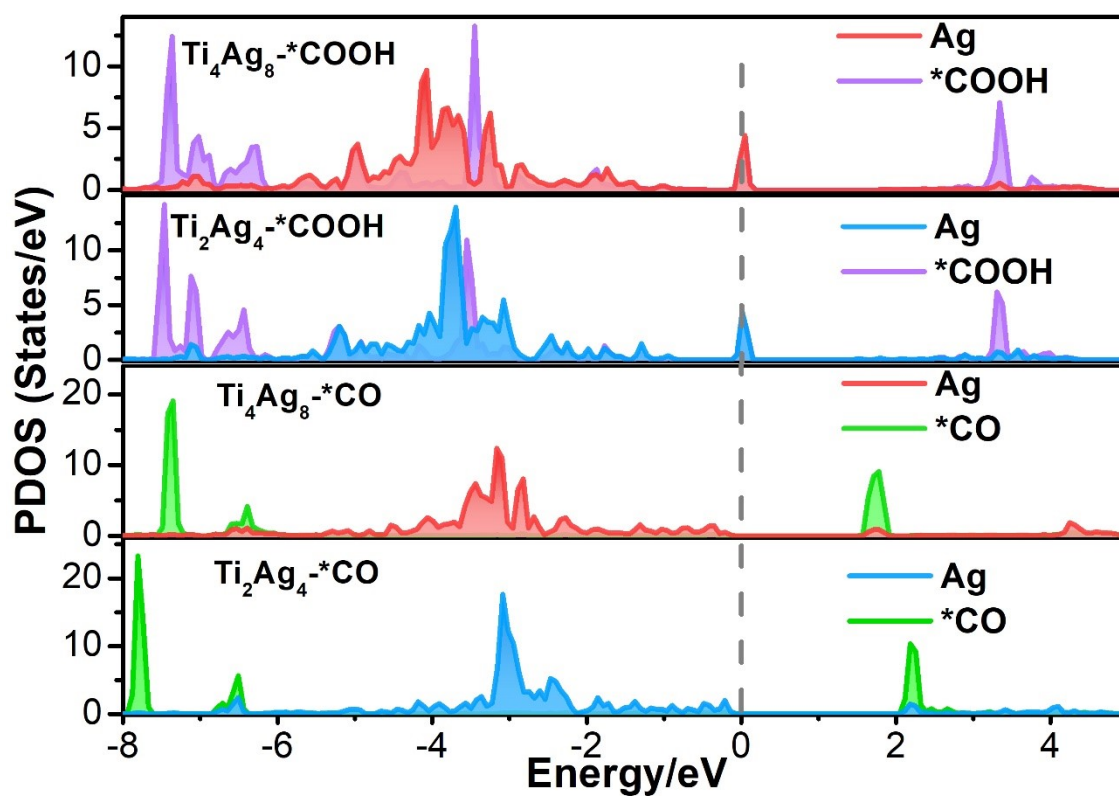

Figure S55. The PDOS after COOH and CO adsorption on Ag atoms.